UNIVERSIDADE
BEIRA INTERIOR

Surrogate Modelling of Propeller Noise in Unsteady Load Conditions

(versão final após defesa)

Pedro Matos Neto

Dissertação para obtenção do Grau de Mestre em

Engenharia Aeronáutica

(mestrado integrado)

Orientador: Prof. Doutor Pedro Vieira Gamboa

Outubro de 2021

Dedicatória

Aos meus pais, que sempre colocaram a minha educação em primeiro lugar.

Agradecimentos

A elaboração deste trabalho só foi possível graças à colaboração e apoio direto ou indireto de algumas pessoas às quais demonstro um sincero agradecimento.

Ao Professor Pedro Gamboa, pela orientação neste trabalho, pelas críticas construtivas, pelas discussões produtivas e pelo rigor que sempre demonstrou. Também pela excecional disponibilidade e dedicação que demonstrou ao longo dos últimos três anos.

A todos os professores, educadores e funcionários que contribuíram para a minha formação e aos quais devo grande parte do que sei.

Aos meus amigos, que me ajudaram a esquecer que estava longe de casa, pelos bons momentos, conversas e aventuras.

A todos familiares e amigos que apoiaram os meus pais e a minha irmã quando foi preciso e eu não estava presente.

Ao meu Pai, à minha Mãe e à minha Irmã pelo apoio, sacrifícios e compreensão. Obrigado por serem as pessoas mais importantes da minha vida.

Resumo

O desenvolvimento recente na tecnologia elétrica tem vindo a ser um catalizador da eletrificação do transporte aéreo que tipicamente requer a utilização de hélices, conhecidas por produzir elevados níveis de ruído. A este facto, juntam-se as crescentes normas anti ruído e a possibilidade de operação em áreas urbanas, o que desperta o interesse no estudo do ruído produzido por hélices.

Esta dissertação apresenta a formulação e implementação de uma ferramenta numérica de análise de ruído produzido por hélices. Esta ferramente é capaz de estimar o ruído produzido por uma hélice em diferentes condições de escoamento e é desenvolvida com foco em problemas de otimização em que o escoamento, posição e velocidade relativas do observador e intervalos das diferentes características geométricas da hélice são especificados.

O código utiliza amostragem por hipercubo latino para selecionar um grupo de hélices representativo do espaço de projeto; De seguida, o nível de pressão sonora para cada uma destas hélices é calculado através de uma formulação da equação de Ffowcs-Williams e Hawkings (FW-H) com dados de carregamento das pás provenientes da teoria do momento do elemento da pá modificada; Estes dados são utilizados para produzir um modelo de Kriging que é disponibilizado ao utilizador para analizar diretamente ou implementar em problemas de otimização.

Os diferentes módulos do modelo foram validados, com sucesso, utilizando dados experimentais e numéricos disponíveis na literatura. Além disso, um caso de estudo onde uma hélice opera na esteira de uma asa foi explorado. Os resultados mostram que há uma clara diferença no ruído produzido em condições de carregamento transiente. Além disso, é observado que a corda, raio, incidência e número de pás podem ser otimizados de forma a reduzir o ruído produzido.

Palavras-chave

Ruído de hélices, carregamento transiente, escoamento perturbado, teoria do momento do elemento de pá, formulação 1A de Farassat, metamodelos.

Abstract

The recent developments in electric technologies have been a catalyst to the electrification of air transport which typically requires the usage of propellers, known to produce high levels of noise. When coupled with tightening noise regulations and the possibility of operation near urban areas, an interest to study propeller noise arises.

This dissertation presents the formulation and implementation of a numerical propeller noise analysis tool. The tool is capable of estimating the noise produced by a propeller under different inflow conditions and is designed to be used in propeller geometry optimisation problems where the inflow conditions, observer position and velocity and the range of propeller geometric characteristics are specified.

The code uses Latin Hypercube Sampling to select a space-filling set of propellers; Then, the overall sound pressure level (OASPL) for these samples is calculated using a formulation of the Ffowcs-Williams and Hawkings (FW-H) equation with loading data from a modified Blade Element Momentum (BEM) theory; A Kriging model is then produced and made available to the user for direct analysis or further implementation in optimisation problems. Validation cases are presented for all modules of the tool and a study case with a propeller operating in a push configuration is analysed.

The different modules of the model were validated against experimental and numerical data from the literature with promising results. In addition, a case study was performed where a propeller operates in the wake of a wing. The results show that there is a clear difference in noise produced under unsteady load conditions. In addition, it is noted that blade chord, radius, incidence and count can be tuned to minimise noise.

Keywords

Propeller noise, unsteady load, disturbed airflow, blade element momentum theory, Farassat 1A formulation, surrogate models.

Contents

List of Figures

List of Tables

Nomenclature

Latin Symbols

a	Induction factor	$-$
B	Number of blades in a propeller	$-$
BPF	Blade Passing Frequency	s^{-1}
c	Propeller blade chord	m
c'	Sound speed of the fluid	$m \cdot s^{-1}$
C_l	Lift coefficient	$-$
C_d	Drag coefficient	$-$
C_a	Axial force coefficient	$-$
C_t	Tangential force coefficient	$-$
CR	Chord Ratio	$-$
D	Propeller diameter	m
D'	Drag force per unit span	$N \cdot m^{-1}$
dS	Element of acoustic source surface	$-$
f	Frequency	Hz
$f = 0$	Acoustic source surface	$-$
F	Prandtl correction factor	$-$
l	Pressure load at the surface	Pa
L	Distributed load	$N \cdot m^{-1}$
L'	Lift force per unit span	$N \cdot m^{-1}$
M	Mach number	$-$
n	Number of query points in a sampling plan	$-$
n_t	Number of samples per rotation	$-$
$OASPL$	Overall Sound Pressure Level	dB
$\{p\}$	Kriging exponent parameter vector	$-$
p'	Acoustic pressure	Pa
p_{ref}	Reference pressure	Pa
PS	Power Spectrum	dB or Pa
PSD	Power Spectral Density	$dB \cdot Hz^{-1}$ or $Pa \cdot Hz^{-1}$
r	Radial position	m

r_{obs}	Distance to the observer	m
r^2	Correlation coefficient	$-$
R	Propeller radius	m
Re	Reynolds number	$-$
S	Relevant area of the aerodynamic body	m^2
t	Observer time	s
TI	Twist Increment	deg
$Thrust$	Propeller thrust	N
u	Local free flow velocity	$m \cdot s^{-1}$
U	Local inflow velocity	$m \cdot s^{-1}$
v	Local propeller induced velocity	$m \cdot s^{-1}$
v_n	Normal velocity of the surface	$m \cdot s^{-1}$

Greek Symbols

α	Angle of attack	deg
θ_P	Local blade incidence	deg
$\{\theta\}$	Kriging linear parameter vector	$-$
μ	Dynamic viscosity of the fluid	$kgm^{-1}s^{-1}$
$\hat{\mu}$	Mean estimate	$-$
ρ	Density of the fluid	$kg \cdot m^{-3}$
σ	Solidity ratio	$-$
$\hat{\sigma}$	Standard deviation estimate	$-$
τ	Source time	s
T	Period	s
ϕ	Local inflow angle	deg
χ	Wake skew angle	deg
ψ'	Azimuth angle	deg
$\{\Psi\}$	Correlation matrix	$-$
ω	Angular velocity	s^{-1}

Other Symbols

$\Box^2$	d'Alembert operator

Subscripts

a	Quantity in the axial direction
L	Loading noise component
r	Quantity in the direction of the observer
ret	Quantity is evaluated at the retarded time
RR	Radius Ratio
t	Quantity in the tangential direction
T	Thickness noise component
x	Quantity in the x axis direction
y	Quantity in the y axis direction
z	Quantity in the z axis direction

List of Abbreviations

2D	Two-dimensional
3D	Three-dimensional
ANOPP	Aircraft Noise Prediction Program
APC	Advanced Precision Composites
ASSPIN	Advanced Subsonic and Supersonic Propeller Induced Noise (Code)
BEM	Blade Element Momentum (Theory)
CAD	Computer Aided Design
CE	Chordwise Elements
CFD	Computational Fluid Dynamics
DFP-ATP	Dunn-Farassat-Padula Advanced Turboprop Prediction (Program)
DFT	Discrete Fourier Transform
DOE	Design of Experiments
EI	Expected Improvement
ESE	Enhanced Stochastic Evolutionary
FFT	Fast Fourier Transform
FW-H	Ffowcs Williams and Hawkings
ISA	International Standard Atmosphere
LHS	Latin Hypercube Sampling
NACA	National Advisory Committee for Aeronautics
NRMSE	Normalised Root Mean Squared Error
RAF	Royal Air Force
RE	Radial-wise Elements
RMS	Root Mean Square
RMSE	Root Mean Squared Error
SMT	Surrogate Modeling Toolbox
UAM	Urban Air Mobility

Chapter 1

Introduction

1.1 Motivation

In the last two decades, there have been several breakthroughs in electric technologies that range from motor design and control to battery design and management and the concepts to implement these technologies. The electrification of air transport will enable more environmentally friendly solutions to the transport of people and cargo such as Urban Air Mobility (UAM) which has been a major research field of several organisations [1].

The operation of these innovative airborne concepts in urban areas raises a series of environmental and social concerns such as the noise produced [2, 3]. Since electric motors are nearly silent, the major sources of noise are the propellers which are necessary to generate thrust and lift.

As these mobility solutions become increasingly predominant, the necessity of developing tools that can predict the noise generated by a propeller under different conditions and configurations increases. Due to the complex nature of the problem at hand, it is expected that the computing time required to accurately produce these predictions makes them infeasible to implement in optimisation problems and parametric analyses where they are needed the most. To overcome this problem, surrogate modelling can be used to approximate the physics based model and produce quick and accurate solutions.

1.2 Objectives

The present dissertation aims to describe the creation of a numerical tool capable of predicting the noise generated in different innovative configurations and designs in a quick and accurate way.

This tool should have the capability to predict the noise generated when the propeller

operates in disturbed airflow caused, for example, by the wing or a pylon in a push configuration. Such consideration is important since an innovative aircraft design often deviates from the traditional fuselage or wing mounted pull propeller. This tool's ability to be easily implemented in aircraft optimisation problems, where propeller noise is a design criterium, is also a fundamental aspect. The tool must also deliver its results quickly to ensure a feasible implementation in optimisation tools and parametric studies in order to facilitate the choice of the ideal propeller radius, blade chord, blade incidence and blade count.

Results will be analysed to better understand the influence of different inflow velocity profiles in the noise emitted by a propeller. The impact of the geometric parameters of interest, as well as the observer's relative position will also be studied.

1.3 Outline

The dissertation is organised in six chapters as follows: Introduction; Literature Review; Methodology; Model Validation; Case Study; and Conclusion.

The first chapter mainly describes the work and its motivation, objectives and importance. The Literature Review focuses on previous research which will serve as the foundation upon which the present work will be built. The Methodology describes the relevant equations and ideas that describe the approach to the problem and their implementation in a python code. In the Validation, results from all the modules are compared to experimental and numerical results from the literature in order to ensure the results are representative of the reality. The Case Study consist of a demonstrative analysis of a propeller operating in the wake of a wing and observed from different relative positions. These results are then analysed and discussed to better understand the importance of the propeller geometry, inflow velocity profile and observer relative position in propeller noise reduction problems. In the Conclusion, the main conclusions and comments of the developed work are presented. Future work is also suggested as a way to entice further work in this topic.

Chapter 2

Literature Review

2.1 Aircraft Propeller Noise

The sound produced by rotating systems such as propellers is known for having a very complex behaviour. Despite its complexity, propeller noise has been of interest since the early days of aviation with the first theoretical work being published in 1919 [4]. By the late 1930s, it was known that the noise generated from blade loading and blade thickness originated from distinct mechanisms. The mechanism of thickness noise was researched by Deming [5] and Ernsthausen [6]. While Ernsthausen qualitatively explained the phenomenon of production of this noise component, it was Deming who mathematically formulated the problem. Deming's results agreed well with the experiments at tip Mach numbers of up to 0.7. The mechanism of loading noise in stationary conditions was studied by Gutin [7] and later extended to forward flight by Garrick and Watkins [8].

Another important source of propeller noise is broadband noise. Unlike the previously mentioned sources which occur at distinct frequencies such as the harmonics of the blade passing frequency (BPF), $BPF = \omega B$, broadband noise is present in all frequencies as exemplified in figure 2.1. This noise source is the result of stochastic sources such as unsteady pressure disturbances caused by turbulence [9]. Although analytical models have been developed to estimate this noise source, due to its stochastic nature, semi-empirical models are typically used. A common simple model is the result of the work of Pegg for helicopters in hover [10] based on previous works from Lowson [11], Hubbard [12], Schlegel [13] and Munch [14]. Another common but considerably more advanced mode was developed by Brooks, Pope and Marcolini [15] and considers five distinct sources: boundary layer turbulence passing over the trailing edge, separated boundary layer and stalled airfoil flow, vortex shedding from laminar boundary layer instabilities, vortex shedding from blunt trailing edges, and turbulent vortex flow that exists near the tips of lifting blades. These considerations are made based on result from experiments using NACA airfoil propeller blades.

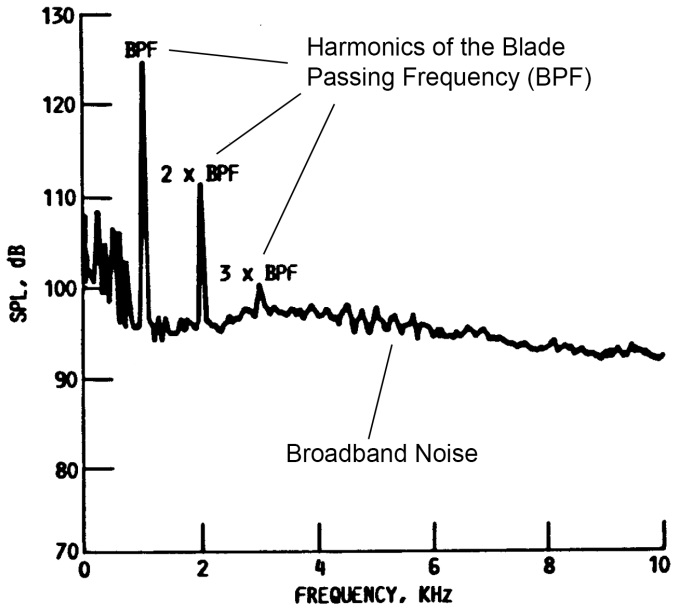

Figure 2.1: Typical noise spectrum of a propeller. Adapted from [16].

Although all noice sources are fundamental to properly predict the sound signature of a propeller, it has been found that for the purposes of overall sound pressure level (OASPL) calculation for propellers in flight, the omission of broadband noise sources does not significantly impact the results [17].

2.1.1 The Ffowcs Williams and Hawkings equation

Despite all these advancements, it was not until 1969, when Ffowcs Williams and Hawkings [18] generalised Lighthill's work [19] to include arbitrary surfaces and motions, that the current era of noise prediction began. The Ffowcs Williams-Hawkings (FW-H) equation (Eq.2.1) was derived by rearranging the Navier-Stokes equations into an inhomogeneous wave equation with a quadrupole source in the volume of fluid surrounding the body and dipole and monopole sources in the surface of the body.

$$\Box^2 p'(x,t) = \frac{\partial}{\partial t}\left[\rho v_n \delta(f)\right]_{ret} - \frac{\partial}{\partial x_i}\left[\vec{l}\,\delta(f)\right]_{ret} + \frac{\partial^2}{\partial x_i \partial x_j}\left[T_{ij} H(f)\right]_{ret} \quad (2.1)$$

where $\Box^2$ is the d'Alembert operator as defined in Eq.2.2, x and t are, respectively, the position and time, ρ is the air density, v_n is the local velocity of the body in the direction normal to the surface (f=0), $\vec{l}$ is the local pressure normal to the surface, T_{ij} is the Lighthill stress tensor, $\delta(f)$ and $H(f)$ are de Dirac delta and Heaviside functions, respectively, and the subscript ret indicates that the quantities should be evaluated in the retarded time.

$$\Box^2 = \frac{\partial^2}{\partial x^2} + \frac{\partial^2}{\partial y^2} + \frac{\partial^2}{\partial z^2} - \frac{1}{c'}\frac{\partial^2}{\partial t^2} \quad (2.2)$$

The work of Farassat, who derived several formulations of the FW-H equation, is one of the main pillars of state of the art noise prediction software. Formulation 1 was first published in 1975 [20] and Formulation 1A in 1980 [21]. These formulations neglect the quadrupole volume sources [22] which do not represent a significant contribution to propeller noise at subsonic speeds [23]. Farassat's 1 and 1A (Eq.2.3) formulations have been implemented in programs such as the Aircraft Noise Prediction Program (ANOPP, [24]), the Dunn-Farassat-Padula Advanced Turboprop Prediction program (DFP-ATP, [25]), WOPWOP, [26] and PSU-WOPWOP [27]. A supersonic formulation, Formulation 3 [28], was also used, in conjunction with Formulation 1A, in the Advanced Subsonic and Supersonic Propeller Induced Noise (ASSPIN) code [29].

$$\begin{aligned}
p'(\vec{x},t) &= p'_T(\vec{x},t) + p'_L(\vec{x},t) \\
4\pi p'_T(\vec{x},t) &= \frac{1}{c'}\int_{f=0}\left[\frac{\rho\dot{v}_n}{r_{obs}(1-M_r)^2}\right]_{ret} dS + \int_{f=0}\left[\frac{\rho v_n(r_{obs}\dot{\vec{M}}\hat{r}_{obs} + c'M_r - c'M^2)}{r^2_{obs}(1-M_r)^3}\right]_{ret} dS \\
4\pi p'_L(\vec{x},t) &= \frac{1}{c'}\int_{f=0}\left[\frac{\dot{\vec{l}}\,\hat{r}_{obs}}{r_{obs}(1-M_r)^2}\right]_{ret} dS + \int_{f=0}\left[\frac{l_r - \vec{l}\,\vec{M}}{r^2_{obs}(1-M_r)^2}\right]_{ret} dS \\
&\quad + \frac{1}{c'}\int_{f=0}\left[\frac{l_r(r_{obs}\dot{\vec{M}}\hat{r}_{obs} + c'M_r - c'M^2)}{r^2_{obs}(1-M_r)^3}\right]_{ret} dS
\end{aligned} \quad (2.3)$$

where p'_T and p'_L denote, respectively, the acoustic pressure generated due to thickness and loading; v, M, l and r denote, respectively, the surface velocity, local Mach number, pressure loading and distance to the observer. Subscripts n and r_{obs} denote that the property must be evaluated in the normal direction to the surface and in the observer direction, respectively. All integrals are calculated at the surface (f=0).

2.1.2 Noise Prediction Algorithms

In acoustic problems, two instances of time are of interest: the time when the sound is emitted (source time, τ) and the time when the sound reaches an observer (observer time, t). These two times are linked by the sound propagation time, which is a function of the

speed of sound, c' and the distance from the source, r_{obs}. The observer time is calculated by:

$$t = \tau + \frac{r_{obs}}{c'} \quad (2.4)$$

and the source time by:

$$\tau = t - \frac{r_{obs}}{c'} \quad (2.5)$$

Acoustic predictions can follow one of two different approaches using either the observer time or the retarded time as the main reference. Algorithms that calculate the observer time from the source time are referred to as source time algorithms and algorithms that calculate the source time from the observer time are called retarded time algorithms. Although the integrands in the Formulation 1A are required to be calculated in the retarded time (hence the ret subscript), both approaches can be used.

Source time algorithms begin with the choosing of a source position and time of interest. Then, for each point of the mesh at the source time: The observer time must be calculated using Eq.2.4, in addition to the relative position of the observer; The mesh nodes' velocity and acceleration at the source time must be calculated. Once the acoustic pressure is calculated at every mesh node, the acoustic pressure is interpolated in order to be added at a single observer time.

Retarded time algorithms begin with the choosing of an observer time and position of interest. Then, for each point in the propeller blade at the observer time: The source time must be calculated using Eq.2.5, in addition to the relative position of the source; The mesh nodes' velocity and acceleration at the source time must be calculated. Once acoustic pressure is calculated, there are no further steps required.

While both algorithms appear conceptually similar, there is a significant difference in the computing time required depending on the number of points in the observer time and the number of necessary coordinate transformations between the observer and propeller frames of reference. It has been showed that source time dominant algorithms require significantly fewer operations, and therefore computing time, when the number of points on the analysed surface or in the observer time range is large [30]. In Figure 2.2 the number of operations as a function of the number of observer times and required coordinate

transformations are plotted.

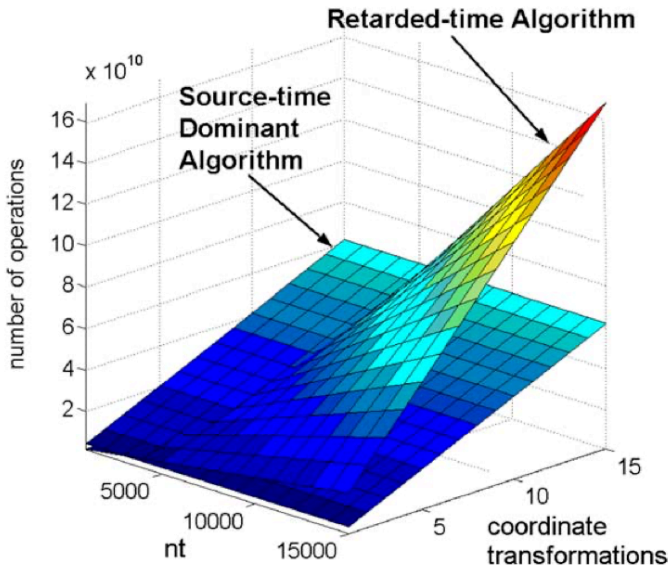

Figure 2.2: Number of operations for source time and retarded time algorithms. Source time resolution is five times the observer time resolution [30].

2.2 Blade Element Momentum (BEM) Theory

One of the required parameters to solve the FW-H equation is blade loading. Blade element momentum (BEM) theory is one of the simplest and most commonly used tools to estimate propeller performance.

The first developments of propeller theory date back to the late 19th century when Rankine and Froude [31] presented a momentum formulation to describe marine propeller propulsion in water. The idea of dividing a propeller blade in a finite number of discrete elements was later presented by Drzewiecki [32] who did not take into account the effect of the air velocity induced by the blade elements. Despite these advancements, it was not until 1935 that the current BEM theory in its classic form was presented by Glauert [33] on the foundation of previous work such as Betz's [34]. This theory combines the notions of blade element theory and blade momentum theory [35] to accurately predict propeller performance. Blade element theory divides the blades into several elements that act independently as two dimensional airfoils and whose aerodynamic coefficients can be calculated based on the local airflow conditions. Momentum theory, assumes that the momentum increase in the propeller plane is a direct cause of the work done by the propeller in the airflow. Momentum theory allows the calculation of the induced velocities which

influence the inflow in the propeller plane and, therefore, also affect the aerodynamic coefficients of each blade element. By coupling these theories iteratively, BEM theory allows the calculation of the aerodynamic forces and induced velocities in the propeller. Classic BEM remains popular in simple mathematical codes due to its conceptual simplicity and effectiveness at describing the complex propeller-fluid interaction.

As with any wing, tip vortices play a significant role in the performance of rotary wings. While originally there were no considerations for this phenomenon in BEM theory, Prandtl developed a correction factor [33] for the induced velocity which allows BEM to model the effect of blade tip vortices. An example of a radial distribution of this correction factor is represented in Figure 2.3 as calculated using Eq.3.15.

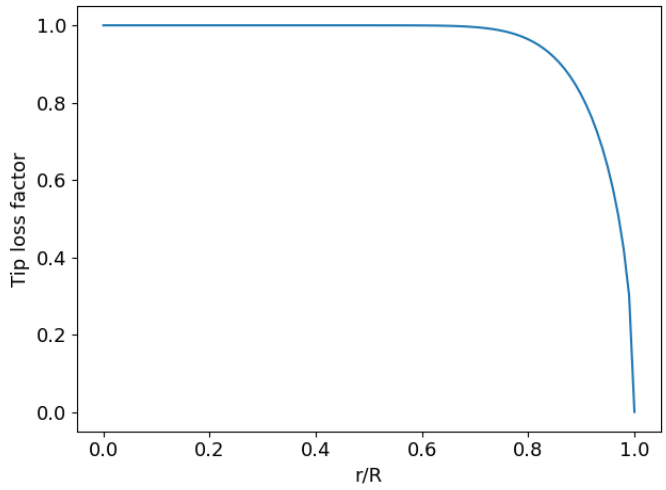

Figure 2.3: Radial distribution of tip loss factor for a two bladed propeller with constant 5 degree inflow angle.

Although BEM theory was developed exclusively considering axial flow, often propellers are faced with skewed or irregular inflow. Corrections to account for these operating conditions in BEM theory were first developed by Glauert [36] for the study of autogyros. Several similar corrections followed such as the works developed by Pitt and Peters [37] and Snel and Schepers [38]. A similar formulation is currently used in BEM theory model in AeroDyn [39], a simulation code to predict the aerodynamic and aeroelastic performance of horizontal axis wind turbines.

2.3 Surrogate Models

optimisation problems usually require repeatedly running a computationally expensive engineering function with different input parameters. Surrogate models are used to emulate the expensive engineering model's behaviour without the slow, expensive computational work and, therefore, reduce optimisation time and costs. These models may also be used to reproduce the behaviour of experimental data of limited sampling size [40]. Essentially, the function of a surrogate model is to approximate the relation between the input and the output of a complex function by establishing a relationship between a set of inputs and outputs.

The Kriging model, originally developed for geostatistics applications such as ore deposit evaluation and mining operation localization optimisation [40], was developed on top of the work of Krige [41] and has seen widespread use due to being usually preferred for most generic applications in addition to engineering problems [42, 43, 44]. Other surrogate modelling techniques such as Polynomials and Radial Basis Functions (Gaussian, Multiquadric, Thinplate, Spline, Cubic and Linear) have also showed great robustness [43]. The adequacy of a surrogate to a certain engineering problem depends on the data set noise, number of samples, number of variables and linearity of the problem.

2.3.1 Design of Experiments

The efficacy of a surrogate is highly dependent on the quality of the samples of the expensive engineering function which are used to train the surrogate. Design of Experiments (DOE) is the process of selecting an optimal sampling plan to best describe the engineering function. Several methods have been developed to generate an evenly distributed efficient sampling plan in the design space. The most common method is Latin Hypercube Sampling (LHS) known for its conceptual simplicity and space filling qualities when optimised [42, 44]. LHS originated from the idea of Latin Squares where a square matrix of size n is filled with n different objects such that each object is never repeated in each row or column. Figure 2.4 is an example of a four object Latin Square. The "Latin" term is inspired by the works of Leonard Euler who used Latin characters to fill the squares [45]. Latin Hypercubes use the same concept by dividing a k-dimensional space in n equally sized bins in each dimension. The k-dimensional space is then randomly sampled such that there

is only one point in each bin row. This characteristic alone is not enough to ensure the

1	4	3	2
3	2	1	4
4	3	2	1
2	1	4	3

Figure 2.4: Illustration of a 4 by 4 latin square.

Latin Hypercube is space-filling - for example, while the diagonal of a matrix does respect the basic principles of Latin Squares/Hypercubes, it is visibly not space filling. Improvements to the original LHS method have been developed such as Orthogonal Array-based LHS [46] and Symmetric LHS [47]. Despite these advancements, the optimal method to ensure that LHS is space filling is through the usage of optimisation algorithms where a space filling criteria optimised. One of the most widely used metrics of sampling plans was initially presented by Johnson *et al* [48]. This criteria begins by calculating the distance between all pairs of points using either the Manhattan norm or the Euclidean norm. Then, a space filling criteria is calculated using the distance between points and number of points at each distance [49]. While this space filling criteria by itself has no meaning, it can be used to compare two different sampling plans.

Adaptive sampling plans [50] are a modern alternative to LHS that uses space-filling criteria to dynamically update the sampling plan and the surrogate. The Expected Improvement (EI) criteria selects the next sampling location that is expected to improve the surrogate model the most [42, 50, 51]. This improvement could be local, to increase fidelity near an area of interest - a local minimum or maximum, for example - or global to increase the overall quality of the surrogate. While these sampling plans tend to offer more efficient use of computing time by only requiring the calculation of points from the engineering function until a stop criteria is met, LHS tends to be preferred for most generic problems due to its simplicity.

Chapter 3

Methodology

3.1 Sound Pressure Calculation

3.1.1 The Farassat 1A formulation

Farassat's 1A formulation as presented by Brentner [26] (Eq.2.3) is used to calculate acoustic pressure in a given observer position and time instant. Since this expression requires detailed pressure data on the source's surface, prior computationally expensive simulations are required. To overcome this, compact formulations can be developed where the distributed pressure blade load is simplified to a distributed radial-wise load [52], as represented in the diagrams of Figure 3.1. The compact approach was applied to the loading term of Eq.2.3, and the resulting formulation is:

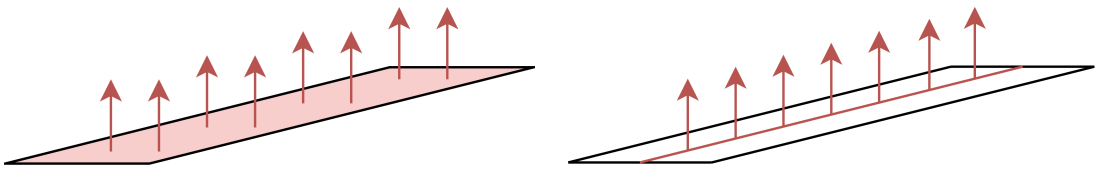

(a) Pressure load. (b) Distributed load.

Figure 3.1: Blade load case simplification.

$$
\begin{aligned}
p'(\vec{x},t) &= p'_T(\vec{x},t) + p'_L(\vec{x},t) \\
4\pi p'_T(\vec{x},t) &= \frac{1}{c'}\int_{f=0}\left[\frac{\rho \dot{v}_n}{r_{obs}(1-M_r)^2}\right]_{ret} dS + \int_{f=0}\left[\frac{\rho v_n (r_{obs}\dot{\vec{M}}\hat{r}_{obs} + c'M_r - c'M^2)}{r_{obs}^2(1-M_r)^3}\right]_{ret} dS \\
4\pi 4\pi p'_L(\vec{x},t) &= \frac{1}{c'}\int\left[\frac{\dot{\vec{L}}\hat{r}_{obs}}{r_{obs}(1-M_r)^2}\right]_{ret} dy + \int\left[\frac{L_r - \vec{L}\vec{M}}{r_{obs}^2(1-M_r)^2}\right]_{ret} dy \\
&\quad + \frac{1}{c'}\int\left[\frac{L_r(r_{obs}\dot{\vec{M}}\hat{r}_{obs} + c'M_r - c'M^2)}{r_{obs}^2(1-M_r)^3}\right]_{ret} dy
\end{aligned}
\tag{3.1}
$$

where L and y denote the radial-wise distributed load and the radial position coordinate, respectively.

Since when operating in steady airflow the acoustic conditions are repeated at a period of one propeller rotation, the object of analysis of the methodology is the sound produced during a single rotation of the propeller. As such, the number observer times to be computed will be relatively low. This, coupled with the few coordinate transformations required in the implementation and the fact that retarded time algorithms are conceptually simpler, facilitated the choice of implementing this formulation in a retarded time algorithm.

3.1.2 Overall Sound Pressure Level

Once the acoustic pressure for a given time span has been calculated, the overall sound pressure level (OASPL), which is a measure of the effective acoustic pressure in a logarithmic scale, is calculated [53, 54]:

$$OASPL = 20 \log_{10} \left(\frac{RMS(p')}{p_{ref}} \right) \quad (3.2)$$

where RMS is the root mean square of the acoustic pressure, p', and p_{ref} is the reference pressure of $10^{-5}\ Pa$. This result is the main output of the model and this methodology.

3.1.3 Power Spectral Density

Although the calculation of Power Spectral Density (PSD) is not the desired output of the methodology, it is an important result for the validation process as experimental results are often expressed in PSD.

Before diving into the concept of PSD, it is important to understand harmonic analysis which is the analysis of a signal through its decomposition on a series of elementary frequencies. The most computationally efficient algorithm to achieve harmonic analysis of a set of discrete data is the Fast Fourier Transform (FFT) presented in 1965 [55] which is a highly efficient algorithm to compute the Discrete Fourier Transform (DFT) [56]. The efficiency of the FFT comes from repeatedly splitting the set of data points in half, which means that the length of the set of data points must be a number of base 2 [56].

The output of the FFT algorithm is an array with the length of the initial data set. For the purposes of harmonic analysis, the output values correspond to the amplitudes of a series of frequencies starting at $0\ Hz$ with the increment of frequency between two different bins, Δf, being calculated with:

$$\Delta f = \frac{1}{\mathrm{T}} \quad (3.3)$$

where T is the period (temporal duration) of the input signal. From the Nyquist theorem, the highest frequency that can be accurately represented corresponds to half the sampling rate [57] and, therefore, only the first half of the output of the FFT is of use. The amplitude of the bins in the first half must be multiplied by 2 to ensure energy conservation.

The PSD can be calculated from the results of the FFT. It is obtained by taking the post processed output of the FFT, known as Power Spectrum (PS), in Pa, squaring it and then dividing by the bin width, Δf. This operation removes the dependency on bin width which is important, especially when analysing random vibration of several different frequencies. The PSD can also be represented in a logarithmic scale (dB/Hz):

$$PSD_{dB} = 10 \log_{10} \left(\frac{PSD_{Pa^2/Hz}}{p_{ref}^2} \right) \quad (3.4)$$

where p_{ref} is the reference pressure of $10^{-5}\ Pa$.

3.2 Blade Element Momentum (BEM) theory

This model divides a propeller blade in a set of independent blade elements which are analysed independently as discrete wings. Each of these elements acts on the airflow by producing axial and tangential forces in addition to inducing axial and tangential velocities to the incoming airflow i.e. the airflow in the propeller plane in case the propeller did not exist.

Although the theory was initially developed with the assumption of perfectly axial flow, this condition may be relaxed if the proper corrections are applied [39]. In this present work, modified BEM theory is applied to non-uniform inflow conditions. Skewed flow corrections are also applied locally at each element. The velocity triangle from Figure 3.2 describes the different velocity components acting in a given blade element and is nec-

essary to determine the local relative velocity, U, and the respective inflow angle, ϕ. The two components of the induced velocity are denoted v_a and v_t for the axial and tangential directions, respectively. The components caused by movement of the propeller in the incoming airflow are $U_a = u_a$ and $U_t = \omega r - u_t$ for the axial and tangent directions, respectively, where u_a and u_t are components of the incoming airflow and ωr is caused by the rotation of the blade element.

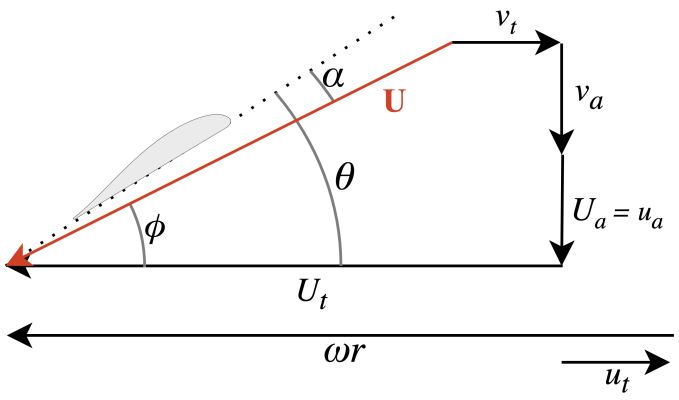

Figure 3.2: Velocity triangle at an arbitrary blade element.

The axial and tangential induction factors are calculated, respectively, with Eqs.3.5 and 3.6.

$$a_a = \frac{v_a}{U_a} \quad (3.5)$$

$$a_t = \frac{v_t}{U_t} \quad (3.6)$$

The local relative air velocity and inflow angle can therefore be calculated by:

$$U = \sqrt{(U_a(1 + a_a))^2 + (U_t(1 - a_t))^2} \quad (3.7)$$

$$\phi = \arctan\left(\frac{U_n(1 + a_a)}{U_t(1 - a_t)}\right) \quad (3.8)$$

The local angle of attack, α, is:

$$\alpha = \phi - \theta \quad (3.9)$$

where θ is the local incidence angle.

The Reynolds number at a blade element is calculated with:

$$Re = \frac{\rho U c}{\mu} \quad (3.10)$$

where ρ is the air density, U is the local relative air velocity, c is the element's chord and μ is the dynamic viscosity of the air.

With the local angle of attack and Reynolds number, the lift and drag aerodynamic coefficients, C_l and C_d, can be sourced using experimental or numerical data. These aerodynamic coefficients are defined, respectively, by Eqs.3.11 and 3.12.

$$C_l = \frac{L'}{\frac{1}{2}\rho c U^2} \quad (3.11)$$

$$C_d = \frac{D'}{\frac{1}{2}\rho c U^2} \quad (3.12)$$

where L' and D' are, respectively, the lift and drag forces per unit span, ρ is the density of the fluid, c is the airfoil chord, and U is the local relative air velocity.

These coefficients are then projected in the axial and tangential directions:

$$C_a = C_l \cos\phi - C_d \sin\phi \quad (3.13)$$

$$C_t = C_l \sin\phi + C_d \cos\phi \quad (3.14)$$

Prandtl's correction factor is implemented to account for blade tip vortices [33]:

$$F = \frac{2}{\pi} \arccos(e^{-\frac{B}{2}\frac{R-r}{r\sin\phi}}) \quad (3.15)$$

where R is the propeller radius, r the local radius and B the number of propeller blades. This correction factor, along with the local solidity ratio, $\sigma = (Bc)/(2\pi r)$, are used to calculate the induction coefficients:

$$a_a = \left(\frac{4F\sin^2\phi}{\sigma C_a} - 1\right) \quad (3.16)$$

$$a_t = \left(\frac{4F \sin\phi \cos\phi}{\sigma C_t} + 1 \right) \quad (3.17)$$

In other to include skewed flow effects the same correction used in AeroDyn [39] was used:

$$a_{a_{skew}} = a_a \left(1 + \frac{15\pi}{32} \frac{r}{R} \tan\frac{\chi}{2} \cos\psi' \right) \quad (3.18)$$

where ψ' is the azimuth angle measured from the most downwind position and χ is the wake skew angle.

This iterative process is initiated by defining initial induction coefficients, $a_a = 0$ and $a_t = 0$, for instance and then the process is repeated until both induction coefficients have converged.

3.2.1 Airfoil Analysis

The aerodynamic coefficients required for Eqs.3.13 and 3.14 can be obtained from many different sources. In this work, the coefficients are either obtained from an open source XFOIL [58] python port integrated in the code or externally through xflr5 [59], an open source analysis tool for low Reynolds numbers that uses XFOIL's airfoil analysis capabilities. Airfoil analyses were performed for a relevant range of Reynolds numbers at a *Ncrit* of 9. This parameter of transition was selected for better representing the behaviour in an average wind tunnel as described in XFOIL's documentation [60]. Before being analysed, airfoils were refined to 200 points, which has been shown to maximize XFOIL's accuracy [61].

It is common for blade sections to reach extreme angles of attach during operation and, while tools such as XFOIL are suitable to estimate an airfoil's aerodynamic coefficients at reasonable angles of attack, they do not perform well at the extremes. As such, these coefficients must be extrapolated using methods such as the method described by Viterna [62], later extended and presented for AeroDyn [63] and extensively described in Airfoil-Prep [64]:

First, the angle of attack, lift coefficient and drag coefficient at stall, respectively, α_s, C_{l_s} and C_{d_s} must be determined. In addition, the minimum value for the angle of attack, lift coefficient and drag coefficient, respectively, α_l, C_{l_l} and C_{d_l} must also be determined.

Then, the following coefficients that describe the shape of the polars is calculated:

$$B1 = 1.8 \tag{3.19}$$

$$B2 = \frac{C_{d_s} - B1 \sin^2 \alpha_s}{\cos \alpha_s} \tag{3.20}$$

$$A1 = \frac{B1}{2} \tag{3.21}$$

$$A2 = C_{l_s} - B1 \sin \alpha_s \cos \alpha_s \frac{\sin \alpha_s}{\cos^2 \alpha_s} \tag{3.22}$$

A parameter to account for the asymmetry of the lift coefficient polar is also defined:

$$C = 0.7 \tag{3.23}$$

The polars are then calculated using the following expressions for each angle of attack range (in degrees):

- $\alpha \in [\alpha_s, 90[$:
  $C_l = A1 \sin(2\alpha) + A2 \cos^2 \alpha$
  $C_d = B1 \sin^2 \alpha + B2 \cos \alpha$
- $\alpha \in [90, 180 - \alpha_s[$:
  $C_l = -C \left(\frac{A1 \sin[2(180-\alpha)] + A2 \cos^2(180-\alpha)}{\sin(180-\alpha)} \right)$
  $C_d = B1 \sin^2(180 - \alpha) + B2 \cos(180 - \alpha)$
- $\alpha \in [180 - \alpha_s, 180[$:
  $C_l = C \cdot C_{l_s} \frac{\alpha - 180}{\alpha_s}$
  $C_d = B1 \sin^2(180 - \alpha) + B2 \cos(180 - \alpha)$
- $\alpha \in [-180, -180 + \alpha_s[$:
  $C_l = C \cdot C_{l_s} \frac{\alpha + 180}{\alpha_s}$
  $C_d = B1 \sin^2(180 + \alpha) + B2 \cos(180 + \alpha)$
- $\alpha \in [-180 + \alpha_s, -90[$:
  $C_l = C \left(\frac{A1 \sin[2(180+\alpha)] + A2 \cos^2(180+\alpha)}{\sin(180+\alpha)} \right)$
  $C_d = B1 \sin^2(180 + \alpha) + B2 \cos(180 + \alpha)$
- $\alpha \in [-90, -\alpha_s[$:
  $C_l = -C \left(\frac{A1 \sin[2(-\alpha)] + A2 \cos^2(-\alpha)}{\sin(-\alpha)} \right)$
  $C_d = B1 \sin^2(-\alpha) + B2 \cos(-\alpha)$

- $\alpha \in [-\alpha_s, \alpha_l[$:

  $C_l = -C \cdot C_{l_s} + \frac{\alpha+\alpha_s}{\alpha_l+\alpha_s}(C_{l_l} + C \cdot C_{l_s})$

  $C_d = C_{d_l} + \frac{\alpha+\alpha_l}{-\alpha_s-\alpha_l}(C_{d_s} - C_{d_l})$

As an example, the aerodynamic coefficients for the RAF 6 airfoil were extrapolated using this method and are represented in Figure 3.3.

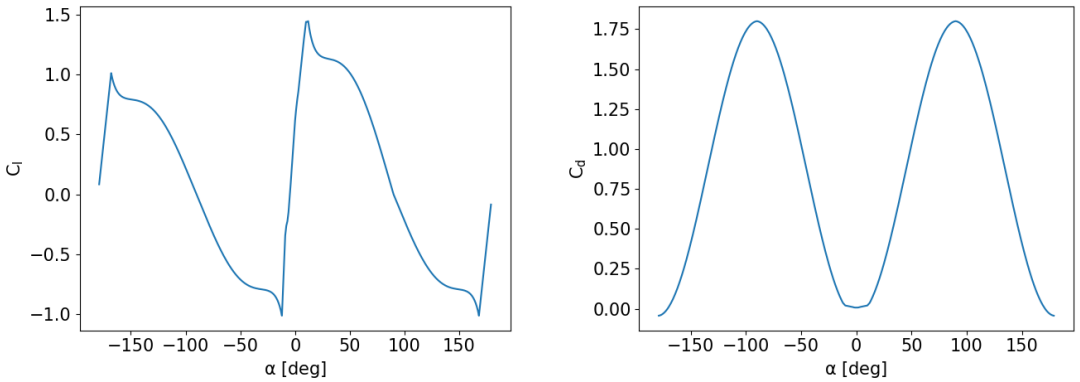

(a) Lift coefficient.

(b) Drag coefficient.

Figure 3.3: Extended aerodynamic coefficients for the RAF 6 airfoil at $Re = 350000$.

3.3 Surrogate Model

The computational time required to solve the previous models thousands of times for every propeller-observer-inflow combination is considerably high. In order to feasibly apply the methodology to real engineering situations, the creation of a more time efficient surrogate is fundamental. The construction of a surrogate model comprises three different stages [42]. First, a set of sample locations must be selected; Secondly, the surrogate model is constructed from the sampled values of the engineering model on the sample locations previously selected; Lastly, the surrogate is validated against the original model.

3.3.1 Latin Hypercube Sampling (LHS)

To construct a Latin Hypercube, the design space is divided into a series of bins of equal space. Then, a point is placed in each bin so that the projection of two given points along an axis does not coincide, this characteristic is called stratification. This method yields a random stratified sampling plan but it does not guarantee an evenly filled design space.

One way to overcome this drawback is the usage of a quality criterion to evaluate the sampling plan and implement an optimisation routine to seek an optimal Latin Hypercube.

The construction and optimisation of the Latin Hypercube was done using the Surrogate Modelling Toolbox (SMT) open-source python package [65]. The optimisation criteria used was the Enhanced Stochastic Evolutionary (ESE) algorithm which has been found to achieve better space-filling metrics while being more efficient than other algorithms [66].

It is recommended that surrogate models operate in the $[0, 1]$ domain for every variable [42]. Therefore, two versions of the same LHS must be created: One in the surrogate domain and one in the engineering function domain. The transformation between the two LHS is linear, as described in Eq.3.24, to ensure the space filling qualities of the LHS remain unchanged between sampling plans.

$$x_{surrogate} = \frac{x_{engineering} - \min(x_{engineering})}{\max(x_{engineering}) - \min(x_{engineering})} \tag{3.24}$$

where $x_{surrogate}$ is the variable value in the surrogate design space and $x_{engineering}$ is the variable value in the engineering function design space.

As an example, let there be an engineering variable with design space $[3, 9]$; The relationship between the upscaled LHS and the surrogate LHS is presented in Figure 3.4.

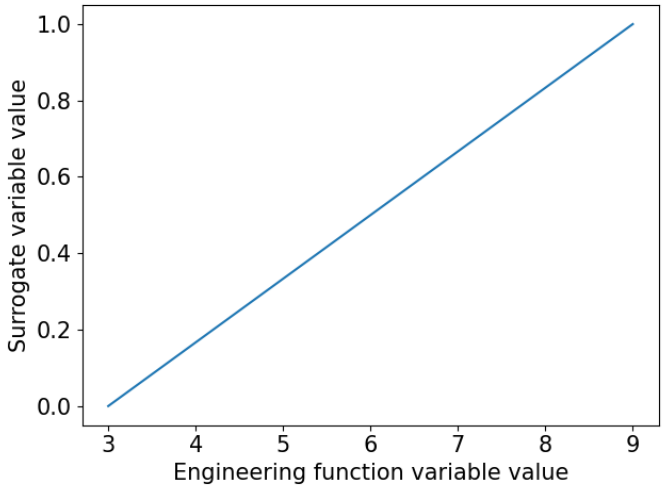

Figure 3.4: Transformation of a variable's range to suit the surrogate.

3.3.2 Kriging

The Kriging model uses the basis function in Eq.3.25 which is similar to the Gaussian basis function differing in the fact that Kriging allows different widths of the basis function, θ, and exponents, p, to every variable. The building of a Kriging model involves selecting the set of values for θ and p that provides the best estimate of the engineering function.

$$\psi^{(i)} = \exp\left(-\sum_{j=1}^{k} \theta_j |x_j^{(i)} - x_j|^{p_j}\right) \quad (3.25)$$

The formulation of the ordinary Kriging as used for interpolation is described below:

Let there be a set of n sample locations, $\{X\} = \{\{x\}^{(1)}, \{x\}^{(2)}, ..., \{x\}^{(n)}\}$ and $\{Y\}$ be the function that generates the sampled values at the locations $\{X\}$ such that:

$$\{Y\} = \begin{Bmatrix} Y(\{x\}^{(1)}) \\ \vdots \\ Y(\{x\}^{(n)}) \end{Bmatrix} \quad (3.26)$$

These samples have a mean, μ, and are correlated together using the basis function from Eq.3.25:

$$\text{cor}\left[Y(\{x\}^{(i)}), Y(\{x\}^{(l)})\right] = \exp\left(-\sum_{j=1}^{k} \theta_j |x_j^{(i)} - x_j^{(l)}|^{p_j}\right) \quad (3.27)$$

where i and l represent two points from $\{X\}$ and k is the number of dimensions of $\{x\}$. By establishing the correlation between all points of the sampling space, a correlation matrix, $[\Psi]$, may be assembled:

$$[\Psi] = \begin{bmatrix} \text{cor}\left[Y(\{x\}^{(1)}), Y(\{x\}^{(1)})\right] & \text{cor}\left[Y(\{x\}^{(1)}), Y(\{x\}^{(2)})\right] & \dots & \text{cor}\left[Y(\{x\}^{(1)}), Y(\{x\}^{(n)})\right] \\ \text{cor}\left[Y(\{x\}^{(2)}), Y(\{x\}^{(1)})\right] & \text{cor}\left[Y(\{x\}^{(2)}), Y(\{x\}^{(2)})\right] & \dots & \text{cor}\left[Y(\{x\}^{(2)}), Y(\{x\}^{(n)})\right] \\ \vdots & \vdots & \ddots & \vdots \\ \text{cor}\left[Y(\{x\}^{(n)}), Y(\{x\}^{(1)})\right] & \text{cor}\left[Y(\{x\}^{(n)}), Y(\{x\}^{(2)})\right] & \dots & \text{cor}\left[Y(\{x\}^{(n)}), Y(\{x\}^{(n)})\right] \end{bmatrix} \quad (3.28)$$

The theory, as defined, allows the correlation of the set of data $\{Y\}$ as described in the correlation matrix, $[\Psi]$. The correlation between a given pair of points depends on their distance, $|x_j^{(i)} - x_j^{(l)}|$, and the parameters θ_j and p_j: θ_j controls the range of a sample

point's influence and p_j controls the curvature of a sample point's influence. Figure 3.5 exemplifies the influence of these parameters.

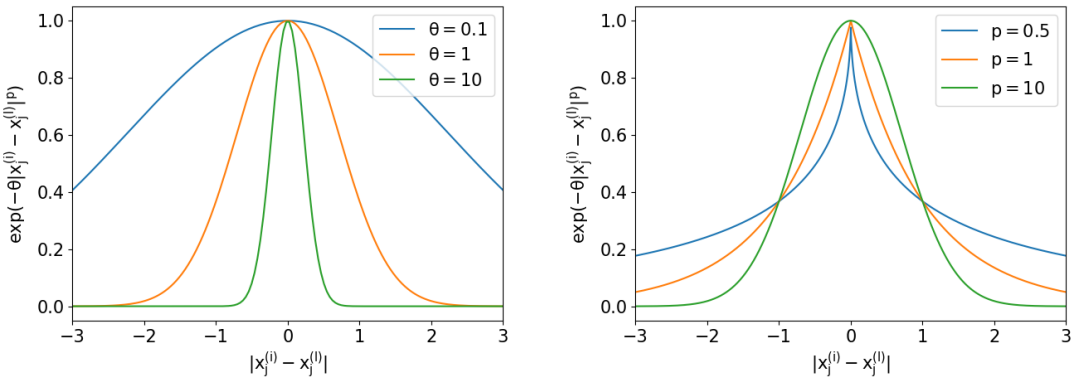

(a) Influence of θ, $p = 2$.

(b) Influence of p, $\theta = 1$.

Figure 3.5: Influence of the Kriging parameters in the correlation.

The construction of the Kriging surrogate itself consists on the selection of the set of parameters for the vectors $\{\theta\}$ and $\{p\}$ that best describes the original function. This is done by maximizing the likelihood function (Eq.3.29) [42] which measures the quality of the fit of a set of sample data and parameters $\{\theta\}$ and $\{p\}$.

$$\ln(L) \approx -\frac{n}{2}\ln(\hat{\sigma}^2) - \frac{1}{2}\left|[\Psi]\right| \quad (3.29)$$

where:

$$\hat{\sigma}^2 = \frac{(\{y\} - \mu\{1\})^T [\Psi]^{-1} (\{y\} - \mu\{1\})}{n} \quad (3.30)$$

The function on Eq.3.29 is non differentiable and presents a very complex landscape leading to the inability to use a traditional optimisation algorithm such as Euler or Powell. Since the function is computationally cheap to calculate, a global search algorithm such as genetic algorithm produces good results [42].

The optimisation method that was implemented in the python code was the "differential_evolution" algorithm implemented in python's SciPy open source library [67] where the algorithm is implemented as published by Storn and Price [68]. The bounds for the variables were set as $\theta_j \in [10^{-3}, 10^2]$ and $p_j \in [1, 3]$ as recommended by Forrester [42]. While the optimisation of the parameters in $\{p\}$ was implemented in the code and successfully tested, it was observed that it slowed down the optimisation process by at least an order of magnitude and the resulting surrogate usually had worse performance than

when p was considered a constant. In addition, the optimised $\{p\}$ values were consistently close to 2. It was therefore concluded that the optimisation of this parameter was not beneficial to the model and all entries of $\{p\}$ were set constant, $p_j = 2$, as suggested by Forrester [42].

Once the parameters have been determined, predictions can be made using the surrogate. A prediction, $\hat{y}$, at a new location, $\{x'\}$, should correlate with the function measurements in the other sampling points using the parameters optimised in the previous step. A correlation vector between the new prediction and the observed function samples may be constructed:

$$\{\psi\} = \begin{Bmatrix} \text{cor}\left[Y(\{x\}^{(1)}), Y(\{x'\})\right] \\ \text{cor}\left[Y(\{x\}^{(2)}), Y(\{x'\})\right] \\ \vdots \\ \text{cor}\left[Y(\{x\}^{(n)}), Y(\{x'\})\right] \end{Bmatrix} = \begin{Bmatrix} \psi^{(1)} \\ \psi^{(2)} \\ \vdots \\ \psi^{(n)} \end{Bmatrix} \quad (3.31)$$

These correlation parameters are then used to produce an estimate at the new point:

$$\hat{y}(\{x'\}) = \hat{\mu} + \{\psi\}^T [\Psi]^{-1} (\{y\} - \hat{\mu}\{1\}) \quad (3.32)$$

where:

$$\hat{\mu} = \frac{\{1\}^T [\Psi]^{-1} \{y\}}{\{1\}^T [\Psi]^{-1} \{1\}} \quad (3.33)$$

3.3.3 Testing the Surrogate

The surrogate is no more than an approximation of the real function. As such, it is fundamental to verify the quality of its estimates. When possible, a fresh space-filling set of data with around 25% of the size of the training data should be used for this purpose [69].

A wide range of different metrics can be used to evaluate a surrogate. Typically, the root mean squared error (RMSE) and its normalised counterpart (NRMSE) in addition to the correlation coefficient (r^2) are used:

$$RMSE = \sqrt{\frac{1}{n} \sum_{i=0}^{n} (y^{(i)} - \hat{y}^{(i)})^2} \quad (3.34)$$

$$NRMSE = \frac{RMSE(\{y\}, \{\hat{y}\})}{\max(\{y\}) - \min(\{y\})} \quad (3.35)$$

$$r^2 = \left(\frac{n \sum_{i=0}^{n} (y^{(i)} \hat{y}^{(i)}) - \sum_{i=0}^{n} y^{(i)} \sum_{i=0}^{n} \hat{y}^{(i)}}{\sqrt{\left[n \sum_{i=0}^{n} y^{(i)2} - \left(\sum_{i=0}^{n} y^{(i)} \right)^2 \right] \left[n \sum_{i=0}^{n} \hat{y}^{(i)2} - \left(\sum_{i=0}^{n} \hat{y}^{(i)} \right)^2 \right]}} \right)^2 \quad (3.36)$$

3.4 CFD Study

The simulation of the velocity profile behind a wing without the influence of the propeller was done through a two-dimensional CFD study in ANSYS FLUENT using the $k - \omega$ SST turbulence model [70]. This turbulence model was used for its versatility and accuracy in many aerodynamic situations such as flow with high curvature and separated flow [71].

The two-dimensional case was studied as opposed to a tridimensional case for simplicity, as a tridimensional study would require a more refined definition of the problem.

3.4.1 Mesh

As is typical for 2D airfoil analysis, a C mesh was used. The meshed area is 6 and 15 airfoil chords in height and width, respectively.

The mesh was made structured to facilitate convergence and accelerate the meshing process. A bias factor was also used to increase refinement closer to the airfoil. Both the number of divisions in every dimension and the bias factor were iteratively adjusted until the y+ value was smaller than 1 and the variation in the NRMSE of the velocity profile between two consecutive iterations was smaller than 3%. Figure 3.6 is an example of a mesh generated using this method.

3.4.2 Boundary Conditions

The inlet was placed in the curved edge of the meshed area and the outlet placed on the vertical edge. Both horizontal edges were left as walls.

The flow velocity vector was set at the inlet by its components and the turbulence intensity

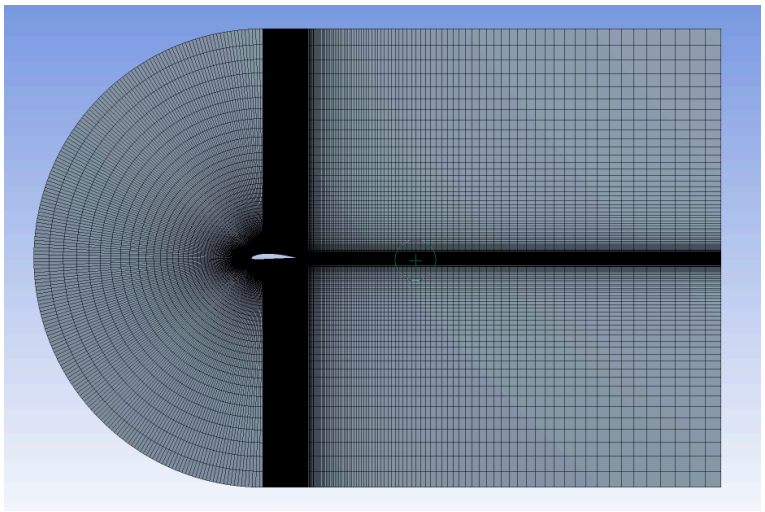

(a) Global view.

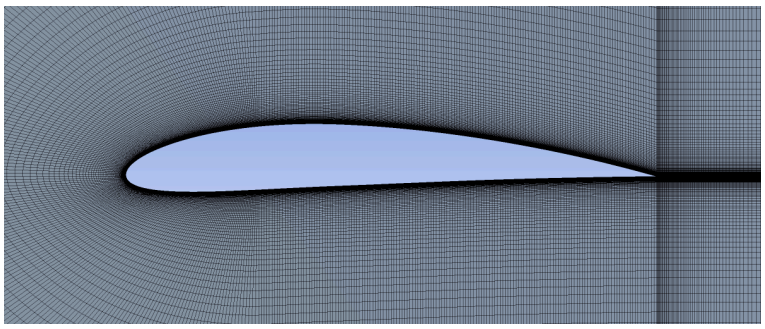

(b) Close up view.

Figure 3.6: Mesh.

and viscosity ratio were set to 5% and 10, respectively. The pressure outlet was set with no back pressure and the same turbulence settings as the inlet. Both walls were set as stationary with no slip and standard roughness.

3.5 Propeller Geometry Measurement

Determining the geometry of a physical propeller is fundamental to reproduce an experiment or when the detailed geometry is not specified by the manufacturer.

Instead of traditional methods such as direct measurement using calipers, it was decided to use a technique where side and top views of the propeller were photographed. This technique allows easy measurement of blade incidence along the radius and consistent measurement of the blade chord.

The measurement setup is described in Figure 3.7. A Nikon D3200 body with the NIKKOR

55-300 mm lens was used which allowed the camera to be placed 4 m away from the propeller as to minimise parallax errors. Both the camera and the propeller were placed at the same height and it was made sure that the propeller was perfectly centered in the camera's viewfinder. The propeller was also placed perpendicularly to the propeller-camera axis.

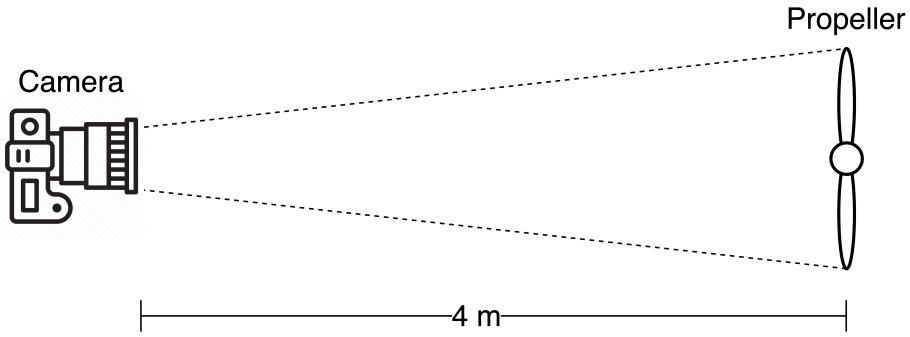

Figure 3.7: Schematic top view of the measurement setup.

The photographs, such as those in Figure 3.8, were manipulated to remove any lens distortion and to facilitate the outlining of the leading and trailing edges of the propeller blades.

(a) Top view.

(b) Side view.

Figure 3.8: APC 15X8E propeller photographic measurements.

These photographs were then imported to CATIA V5 and the horizontal and vertical projections were used to reconstruct the 3D blade shape as demonstrated in Figure 3.9. The chord and incidence of the reconstructed propeller blade was measured at 5% radius intervals from 20% of the radius. The scaling of the images in CAD was done such that the propeller diameter would correspond to experimental measurements.

3.6 Model Implementation

The model was implemented in a python computer code which was made as modular as possible in order to facilitate future improvements to individual modules. Well defined

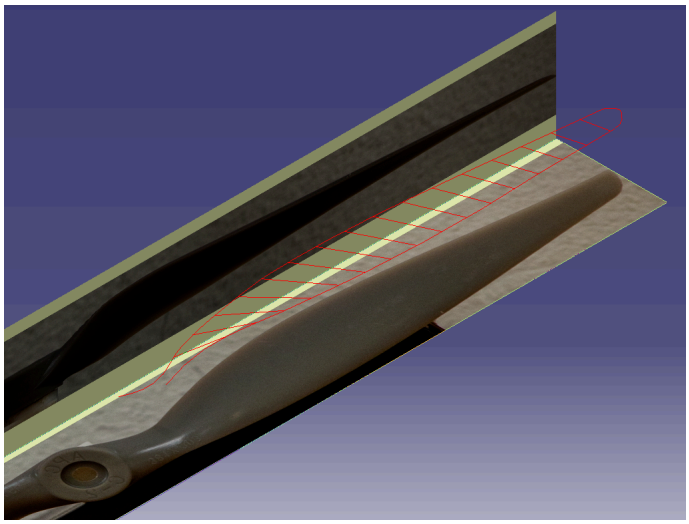

Figure 3.9: Blade geometry reconstruction in CATIA V5.

boundaries were set between the LHS generation module, Kriging optimisation, Kriging prediction, Farassat 1A formulation solver, and blade loading calculation modules.

3.6.1 File Structure

High density problem input and output data such as propeller geometry, airfoil shape, airfoil extended polars, inflow velocity profile and surrogate data are stored using text files to facilitate data management.

The shape of the base propeller blade is defined in a text file, *Propeller.txt*, where it is described as a series of sections characterised by their radial position, chord, twist and airfoil:

r [m]	c [m]	theta[deg]	Airfoil
0.2764432	0.15204376	61.71160658	RAF 6
0.5528864	0.18521694	49.19732226	RAF 6
0.8293296	0.17415921	42.98349791	RAF 6
1.1057728	0.12163500	38.97728919	RAF 6
1.382216	0.02764432	36.84718642	RAF 6

The airfoil shape, which must have been previously normalised, is introduced as a *.dat* file in the Selig format. The blades are assumed not to be swept as this characteristic does not influence significantly the noise production at low Mach numbers and only becomes noteworthy at high sweep angles at transonic helical speeds [9, 72].

The airfoil polars can be calculated and extended in code using an open source XFOIL python port and the airfoil geometry by toggling a setting in the script. It is however recommended to import the extended polars, calculated with a different tool, from an external file. This is done as it was found that under extreme circumstances, such as thick airfoils at low Reynolds numbers, the XFOIL port implemented in code was more susceptible to not converging than xflr5. When imported from an external source, the 360 degree polars must be generated for every blade element (as opposed to every section from the *Propeller.txt* file). These text files, which include the 360 degree lift and drag coefficient polars at a range of Reynolds numbers, are placed in a folder named *Polars* and named *Polars#* where # is the number of the blade element with *0* being the element at the root of the propeller blade. The production of these files is done using a python script that takes xflr5's exported data as an input.

The inflow velocity table is introduced in the *Airflow.txt* file and is structured as follows:

x [m]	y [m]	ux [m/s]	uy [m/s]	uz [m/s]
−8	−2.75	0.00	0.00	75.00
−8	2.75	0.00	0.00	75.00
8	−2.75	0.00	0.00	75.00
8	2.75	0.00	0.00	75.00

The coordinate system used is described in Figure 3.10 where the tip passing plane is the plane xy and the z axis coincides with the propeller axis.

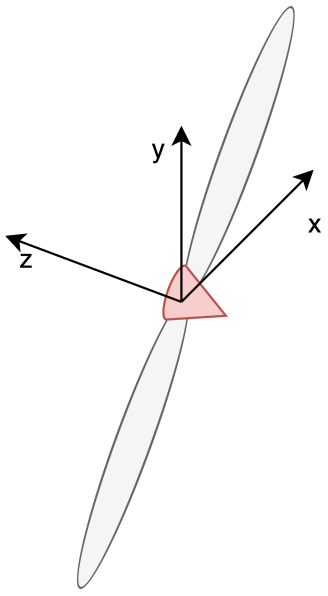

Figure 3.10: Propeller coordinate system.

This velocity table is then linearly interpolated to determine the flow velocity at any given point. Since this example consists of uniform flow, only four corners must be declared. However, in more complex flows, the number of points could be in the hundreds or thousands. The number of points should be as reduced as possible while maintaining noise prediction accuracy in order to maximize interpolation efficiency and therefore improve runtime.

The surrogate data is exported to the *Surrogates* folder where the filename is determined according to the surrogate's design space. Each surrogate data file includes all the required data to produce the Kriging estimates as well as the surrogate's test results and other relevant data. This includes:

- Each design variable's range (or value in case it was kept constant);
- Observer relative position and velocity;
- Vector of Kriging parameters, $\{\theta\}$;
- Vector of Kriging parameters, $\{p\}$;
- Sampling plan locations and values;
- Correlation matrix, $[\Psi]$;
- Testing results: Correlation coefficient, r^2; Root mean squared error (RMSE) and normalised root mean squared error (NRMSE).

3.6.2 Surrogate Construction Script

The main script where the surrogate is constructed has its main logical layout described in Figure 3.11.

The first step is the input, by the user, of the data unavailable from the external files as well as indicating the external files' names. For the initialisation of the incoming airflow object, besides the external airflow file, the density and dynamic viscosity of the air as well as the speed of sound are required; These values may be introduced manually or calculated automatically using the International Standard Atmosphere (ISA) model [73] for a given altitude. The observer relative position and velocity to the propeller must be set using the reference frame of Figure 3.10. The base propeller object is generated from the external

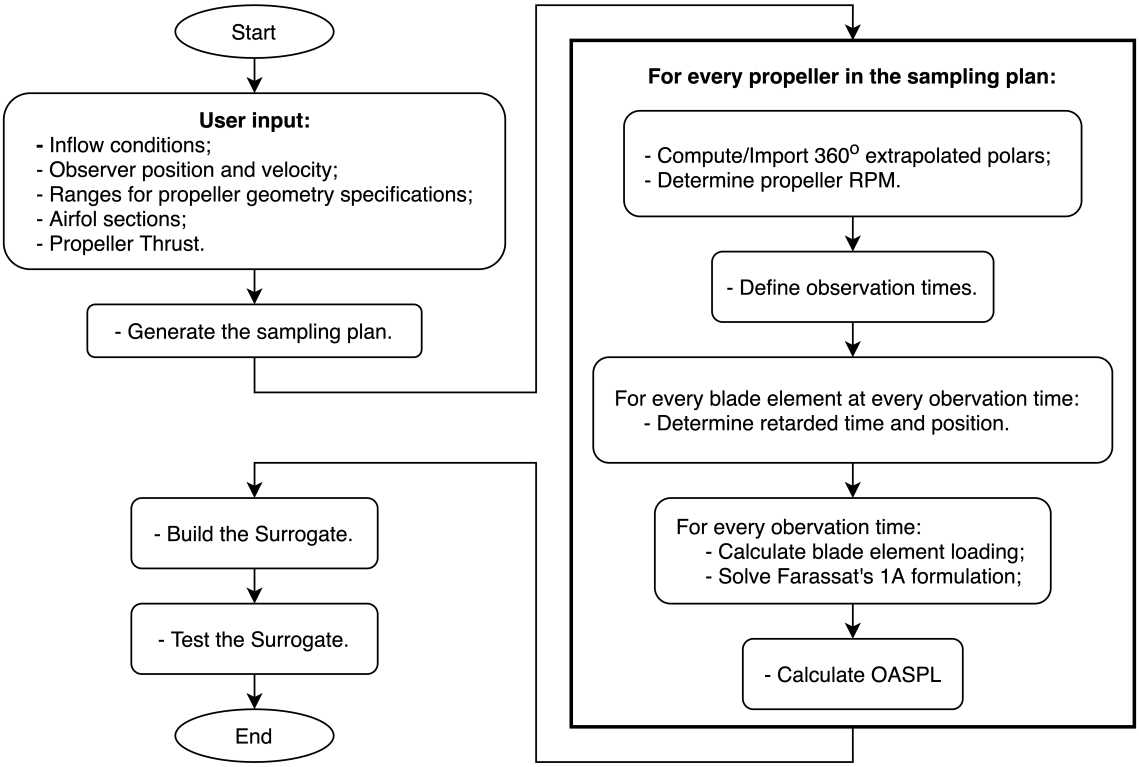

Figure 3.11: Main script layout.

file; Then, the range for the four variables of interest (or value if it is decided for any of them to be kept constant) are set. These variables are: A multiplier for the blade radius of the base propeller; A multiplier for the blade chord of the base propeller; The number of blades and the increase in blade incidence relative to the base propeller (which could be a decrease in case negative numbers are present in the range). The required average thrust generated by the propeller is also required to be specified in the script.

Once the space filling sampling plan with the variables of interest is generated, a loop with a series of steps that lead to the calculation of the overall sound pressure level (OASPL) is performed for each propeller. The OASPL for a propeller at the determined airflow and thrust conditions is calculated using the compact approach to Farassat's 1A formulation (Eq.3.1) whose time derivatives were calculated using first order central finite differences (Eq.3.37) with h being the time taken for the propeller blade to travel a one degree arc, $h = \mathrm{T}/360$, and integrals were calculated using the Simpson method implementation in SciPy [67, 74]. For the purpose of acoustic pressure calculation, propeller blades are divided in a set of 20 radial-wise (RE) and 40 chordwise (CE) evenly spaced elements. These values were found to be the best compromise between accuracy and computational requirements in a series of experiments and is in line with previous works [75, 76]. In

Figure 3.12, the results of a convergence study using the propeller and disturbed airflow from section 5.1 in Position A are represented. It can be concluded that the results converge after 40 chordwise elements and, therefore, this value was selected. Results also begin to converge from, 20 radial-wise elements and, despite there being some improvement from 20 to 30 elements in this particular situation, it was deemed not sufficient taking into account the computing time penalty. The chordwise division is important to properly characterise the curvature of the airfoil, especially near the leading edge [76]. The radial-wise division is more relevant for the calculation of blade loading with BEM theory. The chord, incidence and airfoil at a certain blade element are obtained by linearly interpolating, including the linear interpolation of the airfoil section in case it is not constant, the data from the *Propeller.txt*.

$$f'(x) = \frac{-f(x_{-1}) + f(x_{+1})}{2h} \quad (3.37)$$

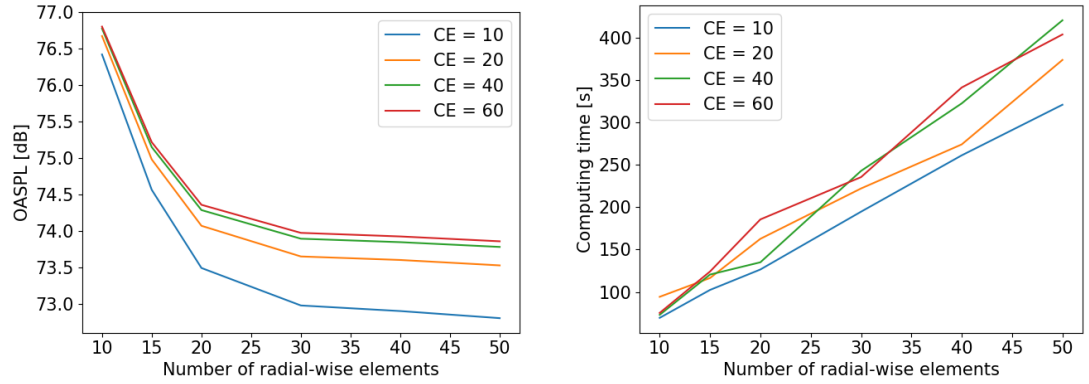

(a) OASPL.

(b) Computing time.

Figure 3.12: Comparison between different element configurations.

Evenly spaced observation times are selected during an entire rotation of the propeller. It is important to use a number of base two in this process to ensure optimal Fast Fourier Transform (FFT) performance when required in the validation process. In Figure 3.13, the results of a convergence study for the number of samples per rotation, n_t, using the propeller and disturbed airflow from section 5.1 in Position A are represented. It was found that results begin to converge at 128 samples per rotation and, although there is some improvement from 128 to 256 samples, it is not significant enough to compensate the exponential increment in computing time. These results are considerably lower than the 512 points suggested by Brentner [76].

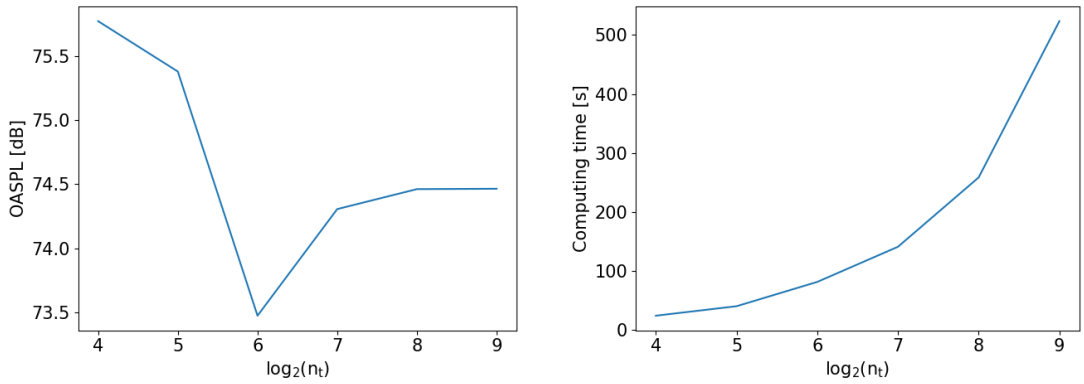

(a) OASPL. (b) Computing time.

Figure 3.13: Comparison between different numbers of observer time samples.

The number of sampling points required for the sampling plan was found to be highly dependent on the range of the variables. The user is responsible for tuning this value such that the surrogate testing metrics are satisfactory. A quality surrogate should have a value of normalised RMSE below 10% and a value of correlation coefficient greater than 0.9 [42].

Chapter 4

Model Validation

Before being suitable to be used in propeller noise estimation problems, the tool must be validated against results available in the literature. In order to better understand the limitations of every module of the model, each module was validated individually. The validation process begins with the validation of the BEM theory implementation in uniform axial flow (steady load condition); Then, results from the BEM theory implementation are compared in skewed flow conditions (unsteady load condition). The results from the noise prediction module are also compared to measurements. Finally, the Kriging surrogate is validated using a typical test function.

4.1 BEM Theory Module in Axial Flow

For the axial flow blade loading case, thrust coefficient comparisons were made with experimental results available in the literature and JBLADE [61, 77, 78] for four different propellers. All calculations in JBLADE were done with 50 blade elements, Prandtl root and tip loss considerations, 3D correction and 3D equilibrium.

4.1.1 Propeller 1

This is a two bladed propeller with 1.76 m diameter that uses the NACA 4415 airfoil. The propeller's chord and twist distributions are represented in Figure 4.1.

The results for the thrust coefficient against the advance ratio are presented in Figure 4.2. These results are compared to experimental data from Adkins [79] and calculations performed in JBLADE. Despite underpredicting the thrust coefficient across all advance ratios, the results follow the same trend as the other sources. At lower advance ratios, when the local angle of attack is lower, there is a considerable underprediction in the thrust coefficient which could be a result of deficient modelling of the airfoil polar beyond the

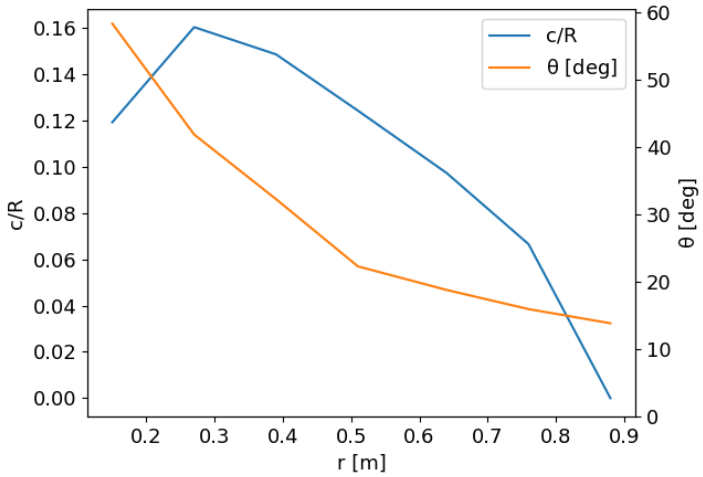

Figure 4.1: Propeller 1, geometry [79].

stall angle. It must be noted that this inflexion point is also present in JBLADE's analysis, although not as predominant, despite JBLADE using more corrections, a more advanced 360 degree polar extrapolation model (developed by Montgometrie [80]) and a post stall model [78].

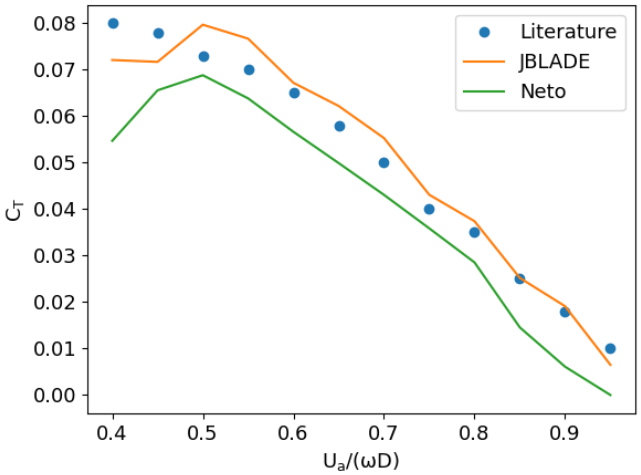

Figure 4.2: Propeller 1, thrust coefficient.

4.1.2 Propeller 2

This is a two bladed propeller with 1.6 m diameter that uses the RAF 6 airfoil. The propeller's chord and twist distributions are represented in Figure 4.3.

The results for the thrust coefficient against the advance ratio are presented in Figure

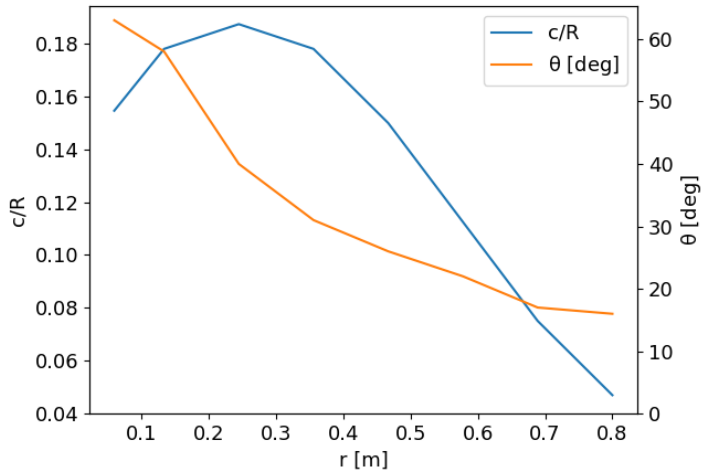

Figure 4.3: Propeller 2, geometry [81].

4.4. These results are compared to experimental data from Xiang [81] and calculations performed in JBLADE.

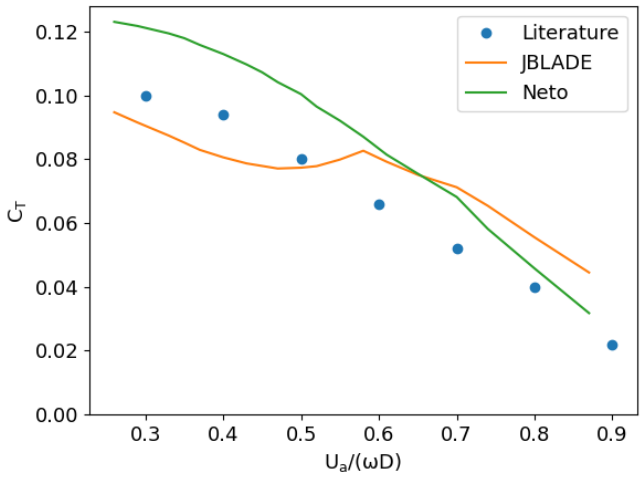

Figure 4.4: Propeller 2, thrust coefficient.

Despite several different trials and experimenting with different settings, the results from JBLADE always presented a non typical behaviour and will therefore be excluded from this comparison. When compared to the experiment, the model's results consistently overpredicted the thrust coefficient, especially at lower advance ratios. The overall tendency of the prediction, however, remains in line with the experiment.

4.1.3 Propeller 3

This is a three bladed propeller with 2.76 m diameter that uses the RAF 6 airfoil. The propeller's chord and twist distributions are represented in Figure 4.5.

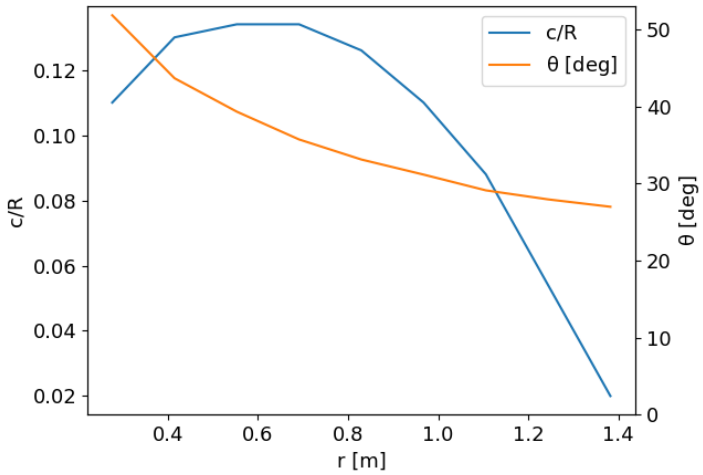

Figure 4.5: Propeller 3, geometry [82].

The results for the thrust coefficient against the advance ratio are presented in Figure 4.6. These results are compared to experimental data from the literature [82] and calculations performed in JBLADE.

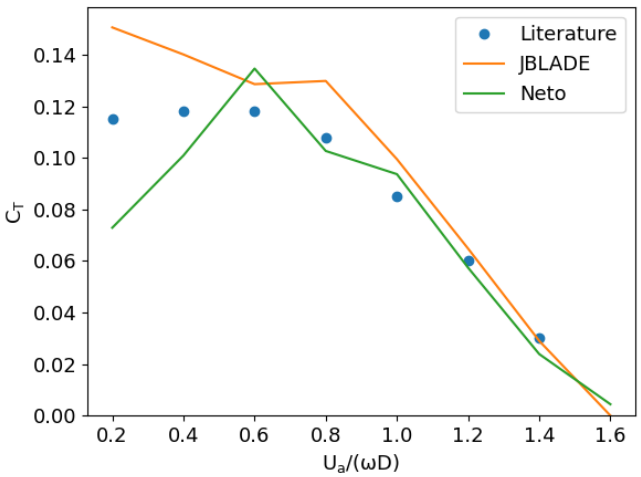

Figure 4.6: Propeller 3, thrust coefficient.

The results from the model are in line with the experiment and JBLADE for advance ratios greater than 0.6. At lower advance ratios, neither BEM theory implementation described the behaviour correctly and the model implemented in this dissertation underpredicted the thrust coefficient results as with Propeller 1.

4.1.4 Propeller 4

This is a three bladed propeller with 3.06 m diameter that uses the CLARK Y airfoil. The propeller's chord and twist distributions are represented in Figure 4.7.

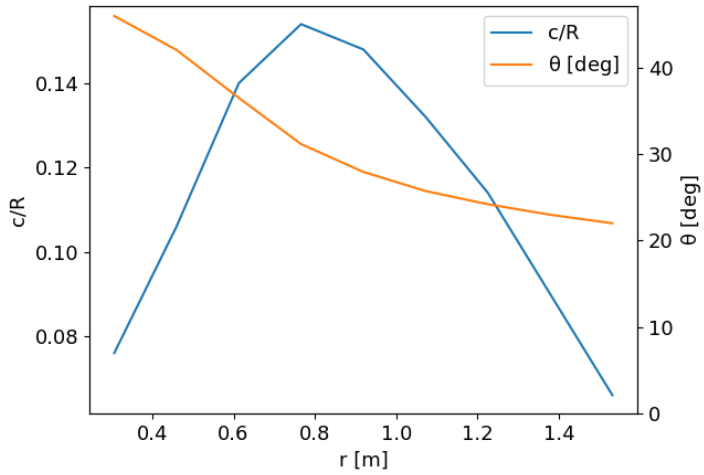

Figure 4.7: Propeller 4, geometry [82].

The results for the thrust coefficient against the advance ratio are presented in Figure 4.8. These results are compared to experimental data from the literature [82] and calculations performed in JBLADE.

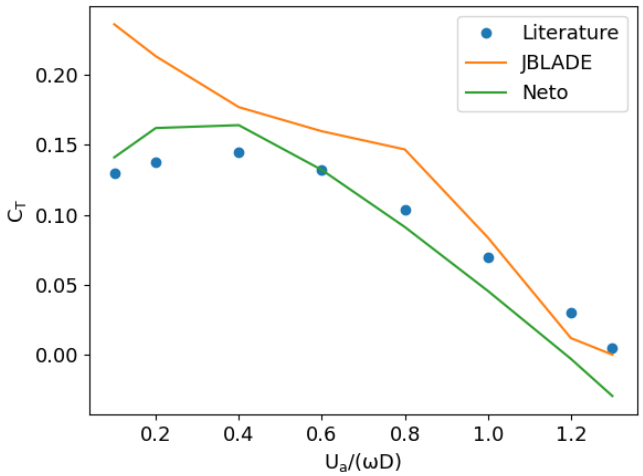

Figure 4.8: Propeller 4, thrust coefficient.

In this case, the model closely follows the experimental results with some overprediction at lower advance ratios and underprediction at higher advance ratios. Overall, the predictions correlate well with the experiment and are, in this case, better than JBLADE's.

4.2 BEM Theory Module in Skewed Flow

The validation for situations of unsteady load was initially intended to be done against skewed flow and wing wake measurements. However, the latter was not possible as the results available in the literature often lack critical details such as propeller geometry or the wake generating body's details which renders the experiment unreproducible.

In this section, comparisons of the thrust coefficient and induction factor for propeller operating in skewed airflow are made.

4.2.1 Case 1

In this case, the thrust coefficient against the advance ratio is compared to experimental results. The experiment consists of testing a special propeller at yaw. The blades of the 1.63 m diameter propeller follow the geometry from Figure 4.9 and use NACA 16- Series airfoils of varying thickness.

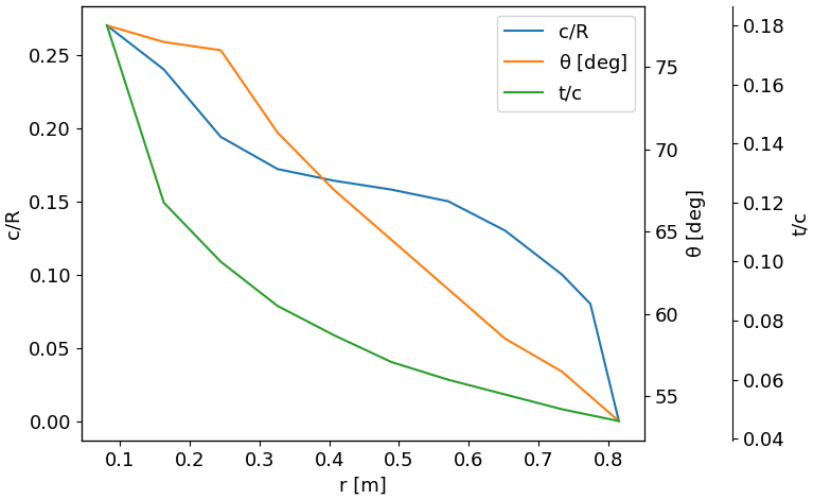

Figure 4.9: Case 1, geometry [83].

The four propeller blades are placed in an unconventional configuration of essentially two two bladed propellers offset 90 degrees and in two different planes as illustrated in Figure 4.10. It is expected for this configuration to produce different results than a conventional four bladed propeller as considered by the computer code. As such, the results will not be compared directly but the change in results from axial to skewed flow conditions will be instead.

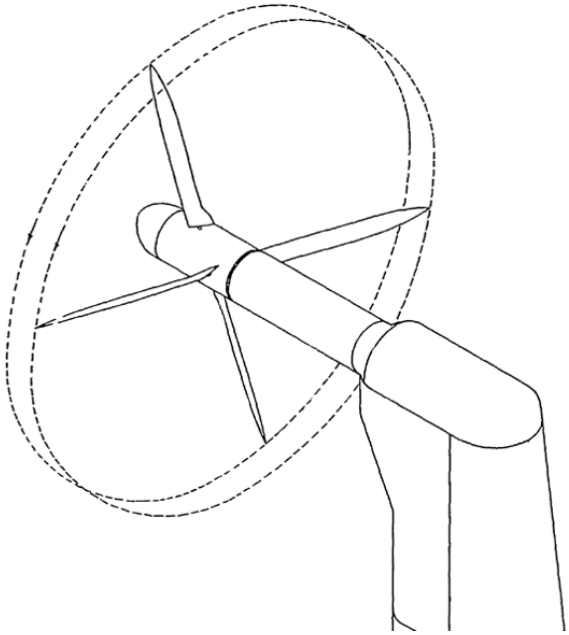

Figure 4.10: Case 1, experimental setup. Adapted from [83].

The results were first compared to the experimental data [83] for the axial flow case. As expected, the results from Figure 4.11 differ considerably, especially at lower advance ratios. It is believed that in the experimental setup the propeller blades in the 2nd plane benefit from the induced wake of the blades in the 1st plane and, therefore do not stall resulting in considerably higher thrust at low advance ratios.

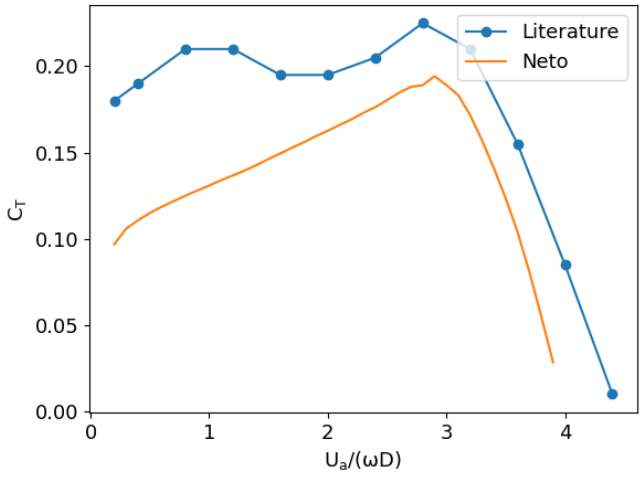

Figure 4.11: Case 1, thrust coefficient in axial flow.

With this phenomenon in mind, the results for the propeller operating at 15 degrees of yaw were compared. From Figure 4.12, it can be concluded that the overall progression of the results is similar; When operating at yaw, both experimental and numerical results suffer a reduction in peak thrust coefficient, increase in maximum advance ratio, and an

overall flattening of the thrust coefficient curve.

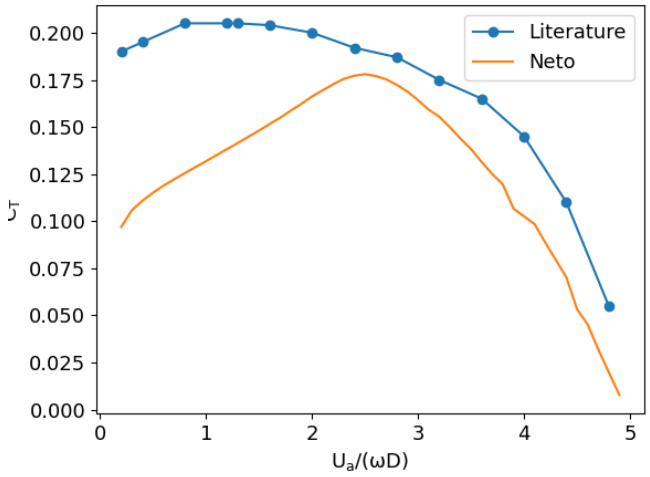

Figure 4.12: Case 1, thrust coefficient at 15 degree yaw.

Although the experimental and numerical curves are very different, the transformations suffered from axial to yawed flow are very similar.

4.2.2 Case 2

Similarly to Case 1, this case consists in the comparison of experimental [84] and numerical curves of thrust coefficient against the advance ratio in axial flow and at yaw.

The blades of the two bladed, 1.22 m diameter propeller follow the geometry described in Figure 4.13 and use NACA 44- Series airfoils of varying thickness.

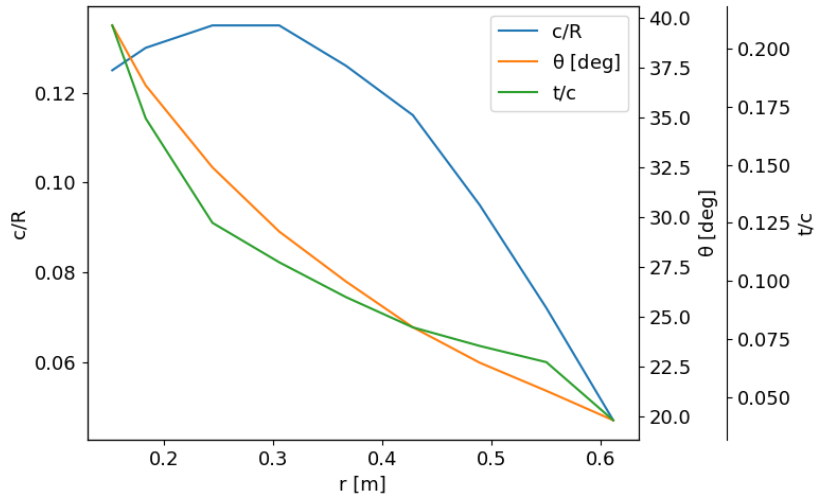

Figure 4.13: Case 2, geometry [84].

From Figures 4.14 and 4.15 it can be concluded that in this particular case, there is little change in the thrust coefficient curve when the airflow is skewed. The numerical results follow the experimental results' behaviour similarly to what was seen in Sections 4.1.2 and 4.1.4.

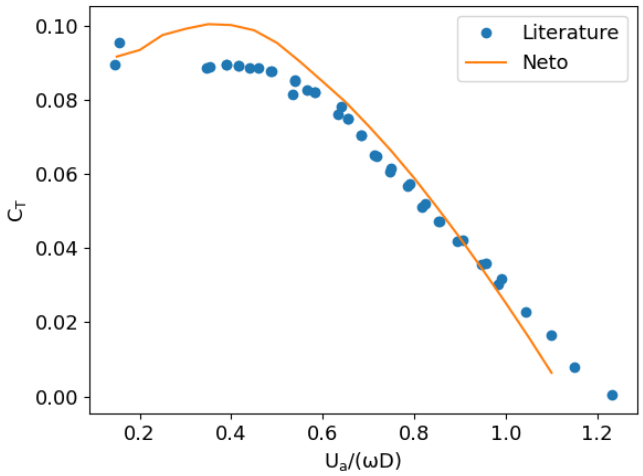

Figure 4.14: Case 2, thrust coefficient in axial flow.

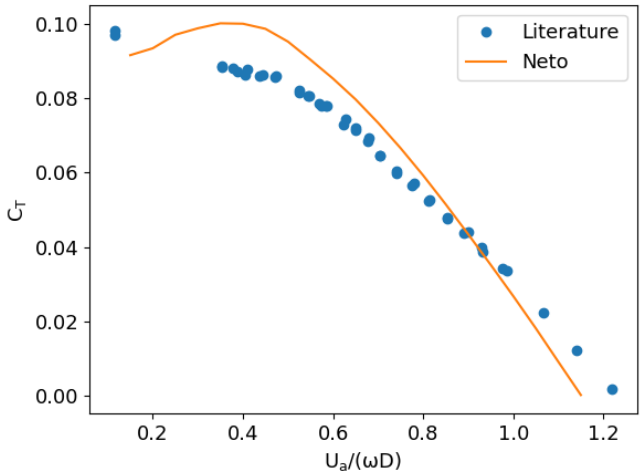

Figure 4.15: Case 2, thrust coefficient at 15 degree yaw.

4.2.3 Case 3

In this case, the axial induction factor is compared to measurements taken from a propeller operating in axial and yawed airflow.

The geometry of the two bladed, 0.5 m diameter propeller is described in Figure 4.16. Since there is no reference to the airfoil section in the original paper, the CLARK Y airfoil

was assumed for being a good generic airfoil for propeller applications.

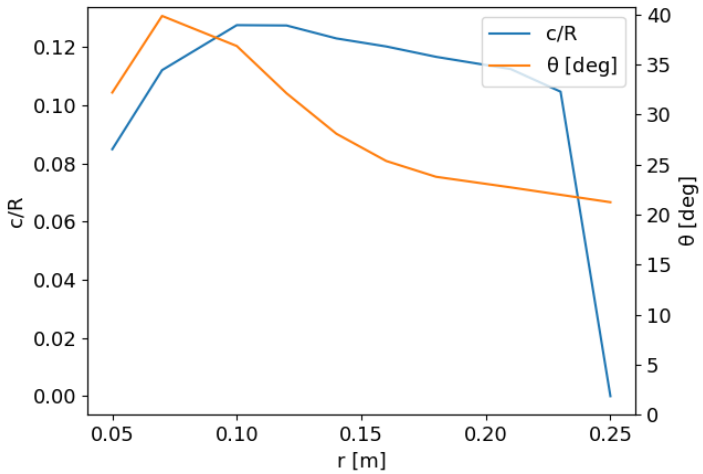

Figure 4.16: Case 3, geometry [85].

As per the experiment, the rotational velocity of the propeller was set at 2756 rpm and the airflow velocity at 20 m/s.

Figure 4.17 illustrates the axial induction coefficient distribution in the disk plane. While the magnitude of the coefficient is similar, it can be seen that the radial position of the peak is more towards the tip in the numerical results. It is possible that this result is caused by the different airfoil selected which would result in a different radial-wise load distribution and therefore in a different local induction factor.

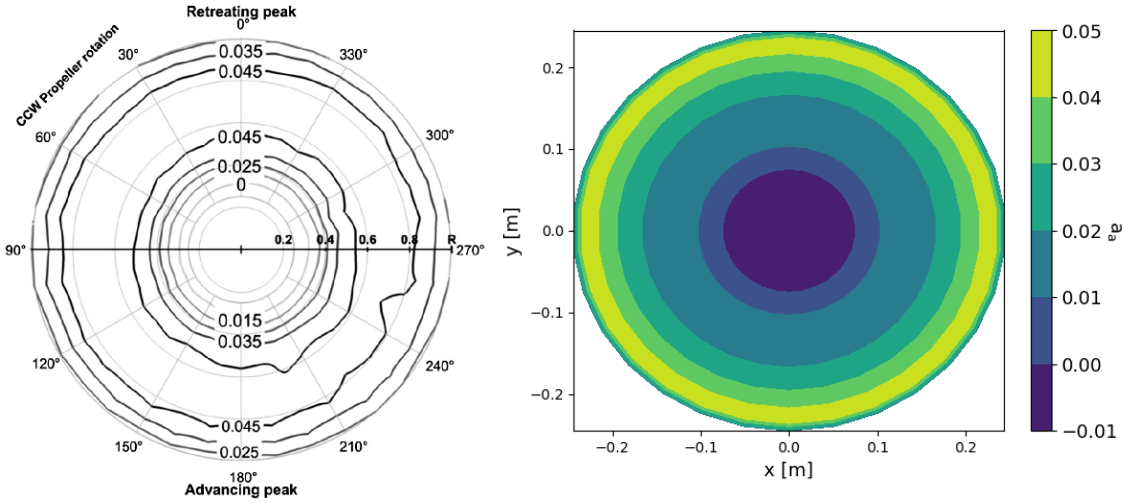

(a) Experimental results [85].

(b) Numerical results.

Figure 4.17: Case 3, induction factor distribution in axial flow.

Comparing the change from the axial flow results (Figure 4.17) to the 20 degree skewed flow results (Figure 4.18), it can be observed that there is a shift of the axial induction

factor peak to the upwind side. The induction factor peak also precedes the upwind peak in both the experimental and numerical studies. On the downwind side, there is a significant decrease in the axial induction factor to the point where it is slightly negative near the root at the opposite side of the high peak. Overall, the numerical model follows the experimental results closely and it can be said that the model accurately describes the reality.

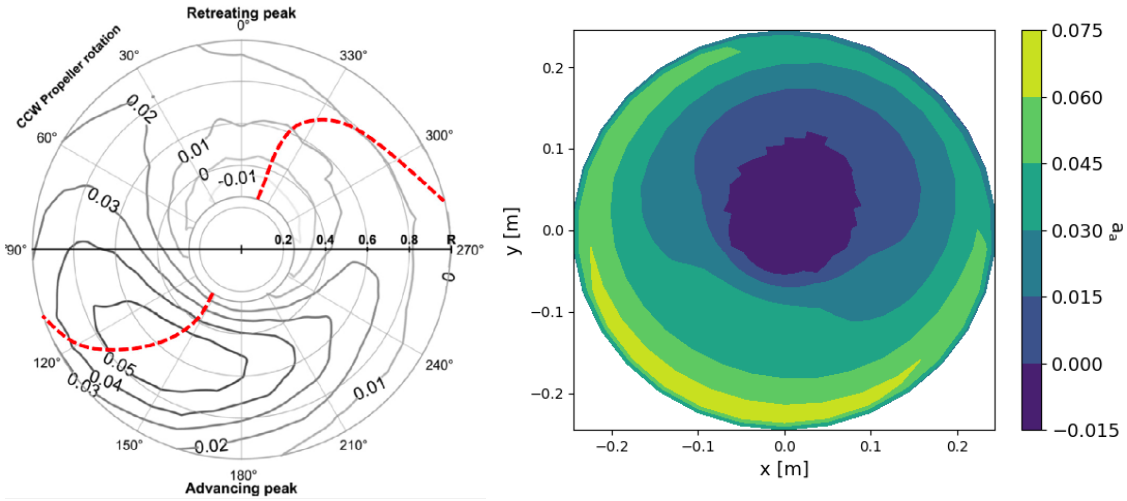

(a) Experimental results [85].

(b) Numerical results.

Figure 4.18: Case 3, induction factor distribution in 20 degree skewed flow .

4.3 Noise Prediction Module

The noise prediction module is the core module of this model. As such, it is fundamental that the results of this module, which also depend on the results of the BEM theory module, are accurate. As such, three different cases were studied.

4.3.1 Case 1

Firstly, noise predictions were compared to experimental measurements and predictions from ANOPP available in the literature [86]. Since detailed geometry of the two bladed 80 inch propeller was not made available, it was decided to use the dimensionless geometry from the Hamilton-Standard 1C1-0 propeller shown in Figure 4.19 and the CLARK Y airfoil modified to the correct thickness.

The three different test conditions considered are described in Table 4.1. For each test

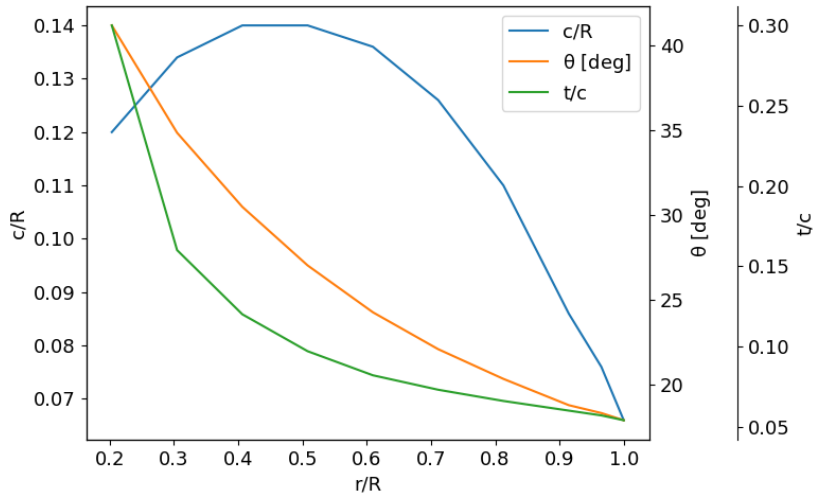

Figure 4.19: Case 1, geometry [82].

condition, noise measurements were taken at a $4\ m$ distance from the propeller hub in the propeller plane and ahead of the propeller, at a 60 degree angle from its axis as represented in Figure 4.20.

Table 4.1: Conditions for test scenarios [86].

Scenario	ω [rpm]	U_a [m/s]	Incidence at .75R [deg]
1	2400	77.2	22.3
2	2700	77.0	22.0
3	2700	77.2	21.2

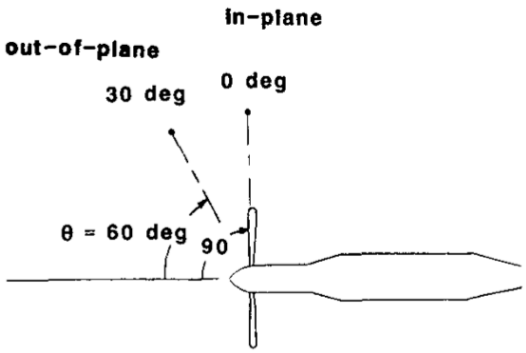

Figure 4.20: Positioning of the microphones relative to the propeller [86].

The results, shown in Table 4.2, are similar to the measured in the experiments and predicted by the more advanced noise prediction code in ANOPP. It must be noted that a certain degree of discrepancy is to be expected since the propeller geometry that was used does not represent the real geometry of the propeller from the experiments. In Scenario 1, where the predicted OASPL differs the most from the literature, the predicted thrust is also 10% greater than the measurements which would increase loading noise and, there-

fore, the overall sound pressure level.

Table 4.2: Comparison of OSAPL predictions to ANOPP and experimental values [86].

Scenario	Experimental [dB]	ANOPP [dB]	Neto [dB]	Error (Neto) [dB]
1 (in-plane)	113.1	113.8	117.6	4.5
2 (in-plane)	123.6	123.2	120.4	-3.2
3 (in-plane)	122.7	122.5	120.1	-2.6
1 (out-of-plane)	108.5	108.1	115.1	6.6
2 (out-of-plane)	115.6	116.3	117.4	1.8
3 (out-of-plane)	115.7	116.2	117.2	1.5

4.3.2 Case 2

In another validation case, the directivity of the power spectral density (PSD) of the first harmonic of the blade passing frequency (BPF) is compared with experimental data from the literature [87].

The propeller used in this experiment was the APC 11 X 8SP. The geometry of this two bladed propeller, assumed to use the CLARK Y airfoil [88], is represented in Figure 4.21.

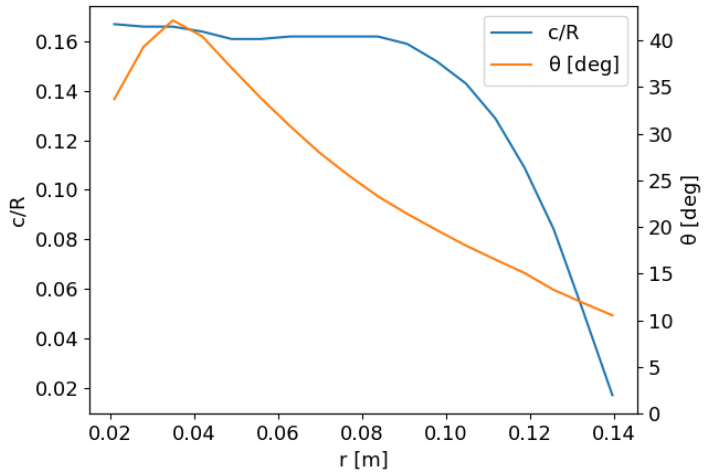

Figure 4.21: APC 11 X 8SP geometry [89].

The results were compared for static operation. However, due to limitations in the BEM theory implementation, it is not possible to have null axial flow velocity. An axial flow velocity of 1 m/s was considered in order to minimise the advance ratio while bypassing the model's limitation.

From Figure 4.22, where 0 degrees coincides with the axial direction ahead of the pro-

peller and 180 degrees coincides with the axial direction behind the propeller, it can be concluded that there is an agreement between the numerical model and the experimental measurements. For the three lower propeller angular velocities, numerical values tend to be up to 3 dB/Hz lower than numerical values. However, at 5500 rpm, the measurements differ considerably from the numerical prediction. This may be a result of experimental errors, since at 5500 rpm the behaviour of the PSD directivity is much different than other angular velocities.

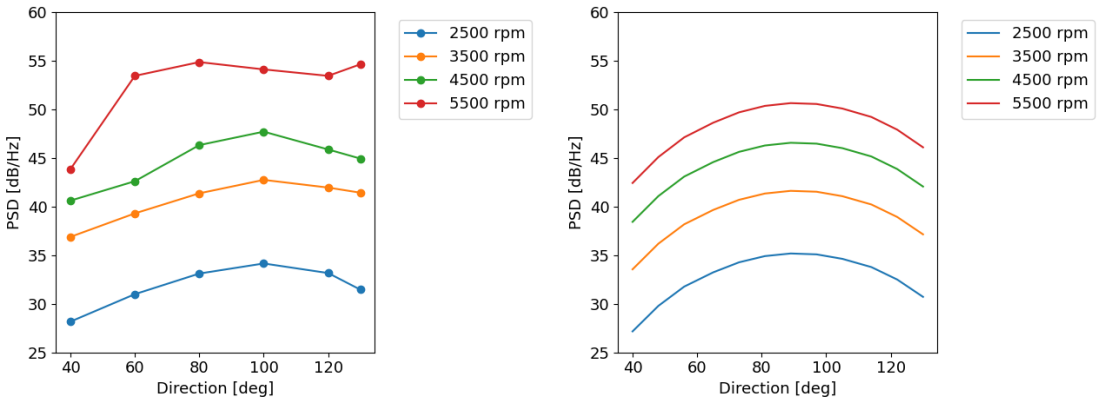

(a) Experimental results [87].

(b) Numerical results.

Figure 4.22: Directivity of power spectral density (PSD) of the APC 11 X 8SP propeller at BPF.

4.3.3 Case 3

This validation case consists in comparing the OASPL produced by an APC 13 X 6.5E propeller in several different positions. The numerical results are compared to experimental results obtained by Marino [90].

Since detailed geometry data was not available and access to this particular propeller was not possible, it was decided to interpolate the geometry from other known APC thin-electric propellers. Using geometry data available on a free access database from University of Illinois Urbana-Champaign [89] and measurements taken from propellers using the method described in Section 3.5, it was concluded that for APCE propellers of the same diameter, the blade incidence at a certain radial position is linearly proportional to the pitch. This situation can be confirmed in Figures 4.23 and 4.24 where the linear regression for 11 and 15 inch propellers at $.5R$ and $.75R$ is shown.

It was also observed that for a given diameter, all propellers of the APC thin-electric family have the same blade chord distribution.

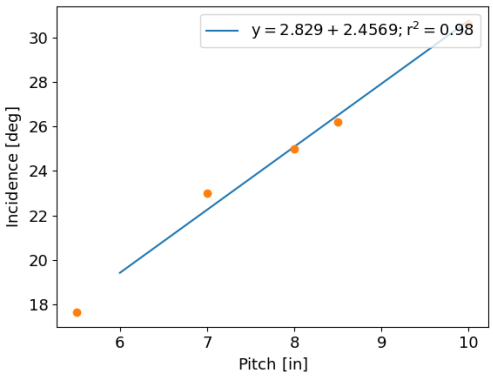

(a) r = 0.5R.

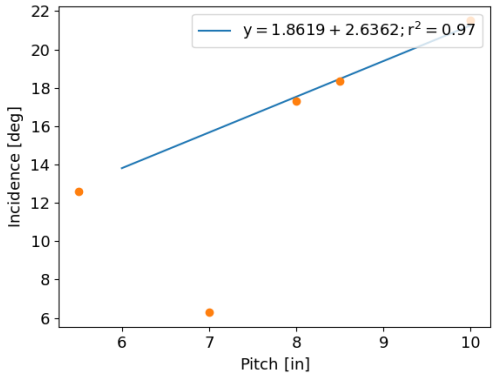

(b) r = 0.75R.

Figure 4.23: Examples of incidence regressions for 11 inch APCE propellers. Data collected from [89].

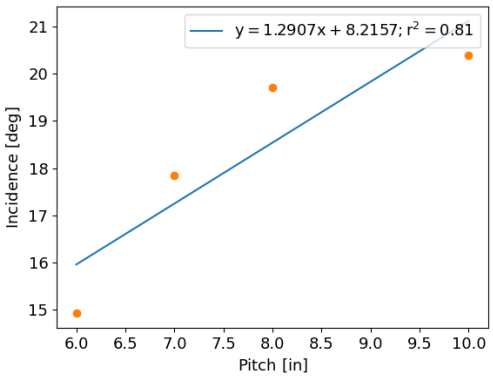

(a) r = 0.5R.

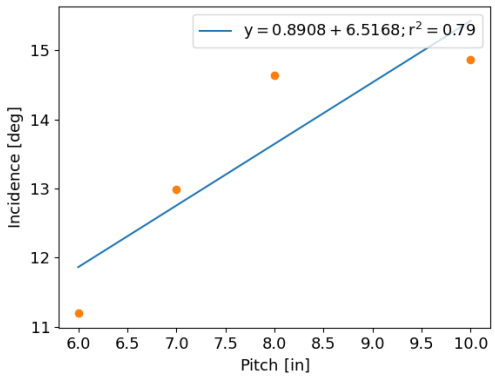

(b) r = 0.75R.

Figure 4.24: Examples of incidence regressions for 15 inch APCE propellers. Data measured with the technique from Section 3.5.

With similar regressions, it was possible to interpolate de geometry data of the APC 13 X 6.5E propeller from the geometry of the APC 13 X 4E and 13 X 10E propellers which were measured using the method from section 3.5. The geometry of the two bladed propeller, assumed to use the CLARK Y airfoil [88], is represented in Figure 4.25.

Although the experiments were conducted in static conditions, due to limitations in the BEM theory implementation, it is not possible to have null axial flow velocity. An axial flow velocity of 0.5 m/s was considered in order to minimise the advance ratio while bypassing the model's limitation. The propeller's angular velocity was set at 2400 rpm.

The noise measurement positions were set according to the frame of reference from Figure 4.26 with the origin at the propeller hub.

The numerical results are compared to the experiments in Figure 4.27. Despite some ex-

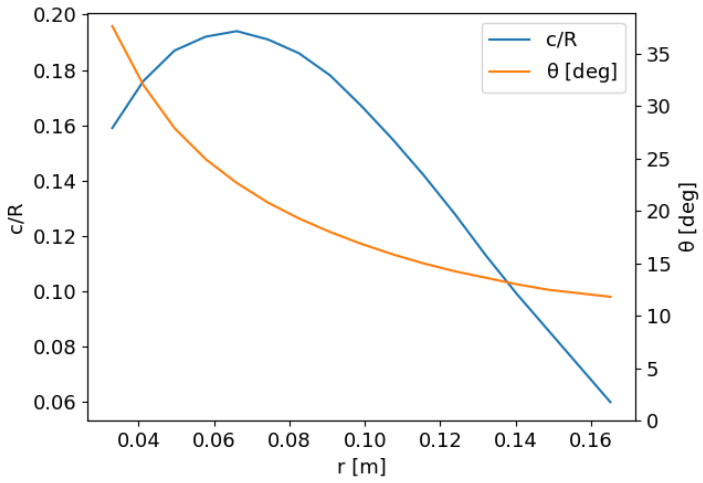

Figure 4.25: APC 13 X 6.5E interpolated geometry.

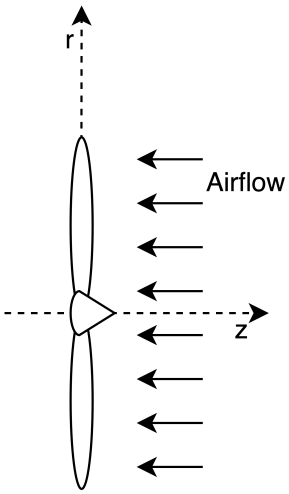

Figure 4.26: Coordinate system.

ceptions, the model's results clearly follow the experimental trend. The largest deviation is observed at the closest measurement point to the propeller ($r = 1\,m$ and $z = 0\,m$) which could potentially be caused by propeller induced turbulence near the microphone which is not modeled. In general, the predictions in the acoustic far-field, which is of more interest in this work, are accurate.

4.4 Kriging Surrogate

The validation of the Kriging surrogate implementation was done by creating and testing the surrogate of a modified version of the Branin function (Eq.4.1) [42].

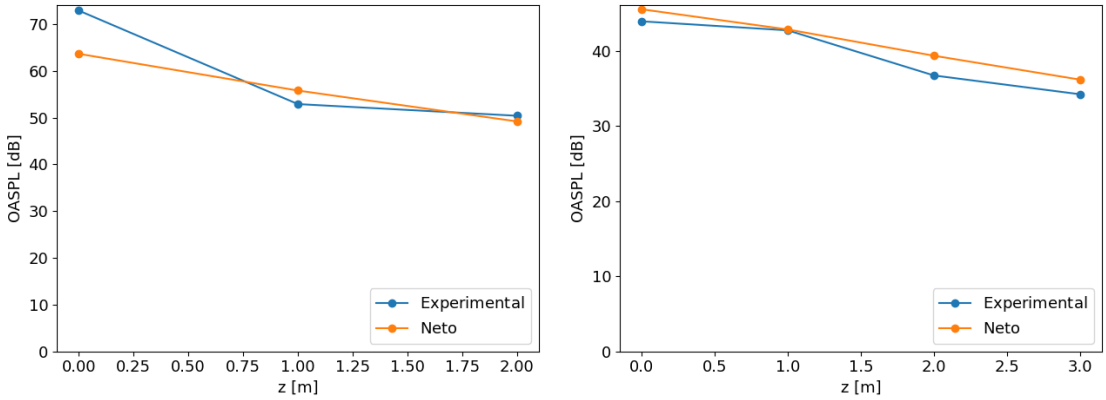

(a) r = 1 m. (b) r = 2 m.

Figure 4.27: Measured [90] and numerical results in different positions.

$$f(x,y) = \left(y - \frac{5.1}{4\pi^2}x^2 + \frac{5}{\pi}x - 6\right)^2 + 10\left[\left(1 - \frac{1}{8\pi}\right)\cos(x) + 1\right] + 5x, \quad (4.1)$$

where $x \in [-5, 10]$ and $y \in [0, 15]$

The testing process included, for several numbers of query locations, n, the construction of the Kriging surrogate and its validation against a set of 20 space filling samples of the modified Branin function. The tests were performed for two different conditions: optimising θ and setting $\{p\}$ as 2, and optimising both $\{\theta\}$ and $\{p\}$.

From Figure 4.28, it can be concluded that the increase in the number of points tends to increase the accuracy of the surrogate. The optimisation of just one set of parameters ($\{\theta\}$) is advantageous as it typically generates better fitting surrogates with less sampling points. In addition, the optimisation of the two sets of parameters ($\{\theta\}$ and $\{p\}$) occasionally generates unfitting surrogates despite having a high number of points.

In Figure 4.29, it can be observed that for the same correlation coefficient, the optimisation of just the $\{\theta\}$ parameters is vastly more efficient and always delivers better results quicker.

Overall, it is concluded that the optimisation of $\{p\}$ is not advantageous in this implementation of the Kriging model. This is not a limitation of the Kriging model itself, but a limitation of the optimisation methodology implemented in the computer code. This result has been expressed by Forrester [42] and is a result of the nature of the parameters in Eq. 3.25. While $\{\theta\}$ is a linear parameter and, therefore relatively easy to optimise, $\{p\}$

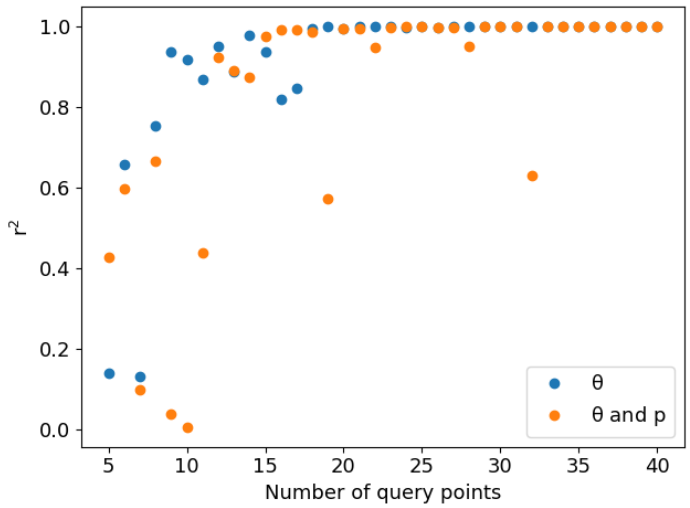

Figure 4.28: Correlation coefficient for different numbers of query points.

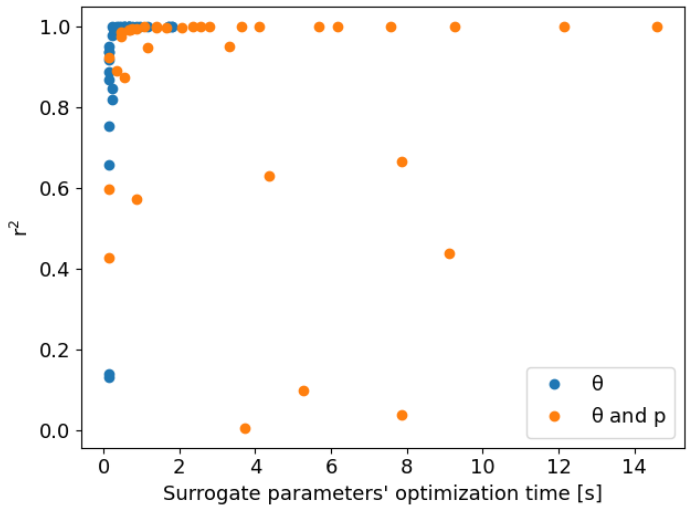

Figure 4.29: Correlation coefficient at different parameter optimisation times.

is an exponent and, therefore its optimisation is difficult, longer lasting and may result in a false optimal such as the outliers from Figure 4.28. As such, it was decided to only optimise $\{\theta\}$.

In Figure 4.30 a comparison between the directly calculation and a surrogate with $\{\theta\}$ optimised and 20 sample points is made. Visually, the two plots are identical and the correlation coefficient of 0.9996 indicates that the surrogate's estimate is a good representation of the original function.

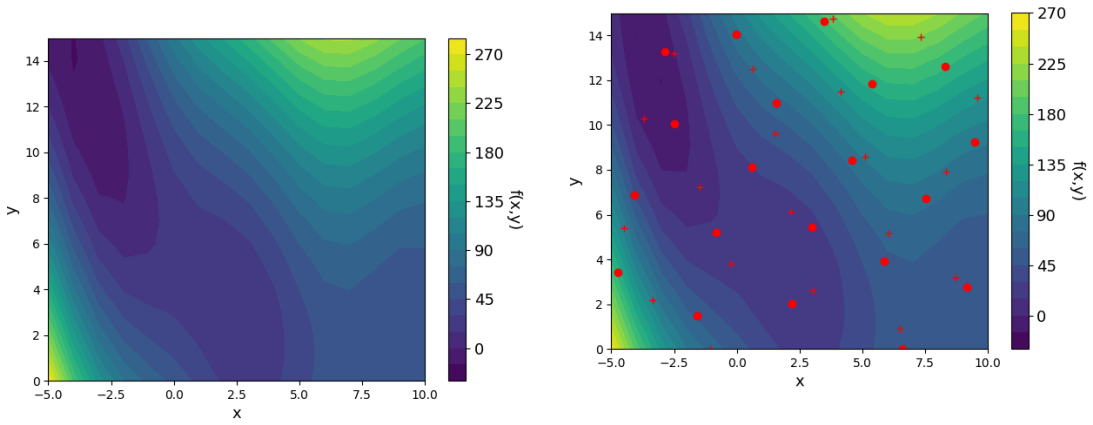

(a) Direct calculation.

(b) Kriging surrogate.
"o" = Sample points; "+" = Valitation points.

Figure 4.30: Modified Branin function.

4.5 Conclusions

The validation cases tested in this chapter show that all modules of the python computer code are reasonably accurate and suitable to be used in noise calculation problems.

In axial flow situations, the thrust coefficient predictions from the model implemented in this dissertation follow both the results from experiments and JBLADE. In skewed flow situations, the thrust coefficient and induction factor predictions are similar to experimental results. It must be noted that, since there is no consistency in the error of the numerical results due to limitations in BEM theory, there is some degree of uncertainty in the results produced using this model.

The noise prediction module proved reasonably accurate in both OASPL calculations and the more rigorous directional PSD calculations showing promising results for both small and large aircraft propellers at different relative positions. There is no consistent tendency to over or underpredict the OASPL results, which leads to a degree of uncertainty in the results produced by the tool. It is likely that this is a result of the inconcistency found in the BEM theory module's results.

The Kriging surrogate also proved effective at emulating the behaviour of a typical test function despite one of the relevant parameters not being optimised.

Chapter 5

Case Study

In order to illustrate the general behaviour of the noise emitted by an aircraft propeller under different conditions and the impact of changing certain propeller design elements, a case study was created.

5.1 Problem Definition

5.1.1 Propeller Geometry

The base propeller uses the blade geometry from the Navy planform 3790, represented in Figure 5.1.

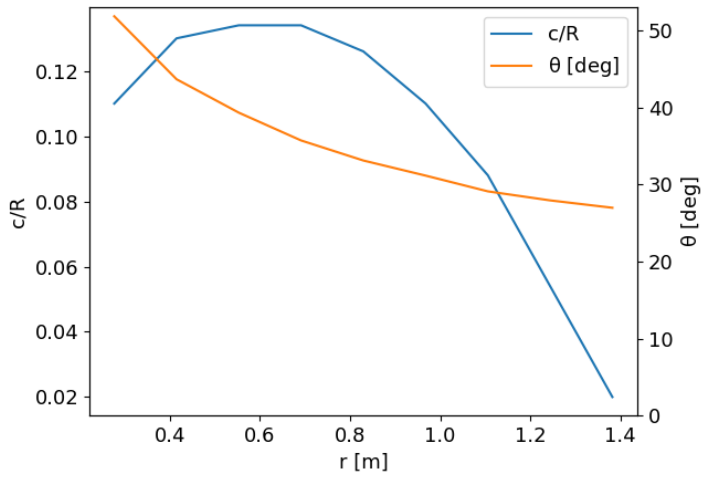

Figure 5.1: Base propeller geometry [82].

The design space for the surrogate's variables are set as in Table 5.1. These boundaries were selected such that the design space would be broad enough to clearly display the influence of each variable but not too broad that the surrogate would face difficulties to emulate the model's behaviour.

Table 5.1: Design space used in the surrogate.

Variable	Lower boundary	Upper boundary
Number of blades (B)	2	6
Chord ratio (CR)	0.5	2
Radius ratio (RR)	0.5	2
Twist increment (TI) [deg]	-10	10

5.1.2 Observer positions

The study was performed at sea level in horizontal flight at 75 m/s. Noise measurements were taken at the points A, B, C and D from Figure 5.2.

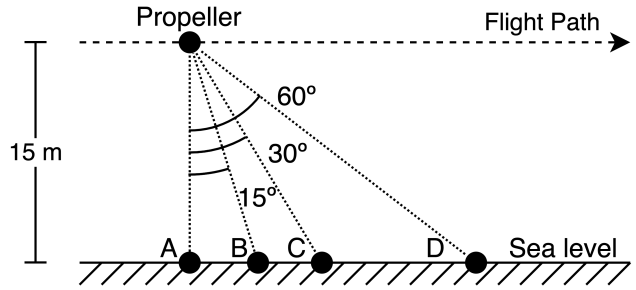

Figure 5.2: Observer positions considered in the case study.

5.1.3 Wake

For the cases where the wake of the wing is required, the propeller was considered to be operating 0.5 m behind the trailing edge of a 1.84 m chord NACA 23013 airfoil wing flying at 75 m/s and 0 degree angle of attack. Using the process described in section 3.4, the velocity profiles from Figure 5.3 were calculated.

5.2 Propeller Noise in Free Stream and Wake

One of the main objectives of this dissertation is for the tool to have the ability to determine the noise produced by a propeller under different inflow conditions. In order to gauge a better understanding of the consequences of operating in the wake of a wing, with the observer in position A, comparisons of the noise produced by the base propeller while

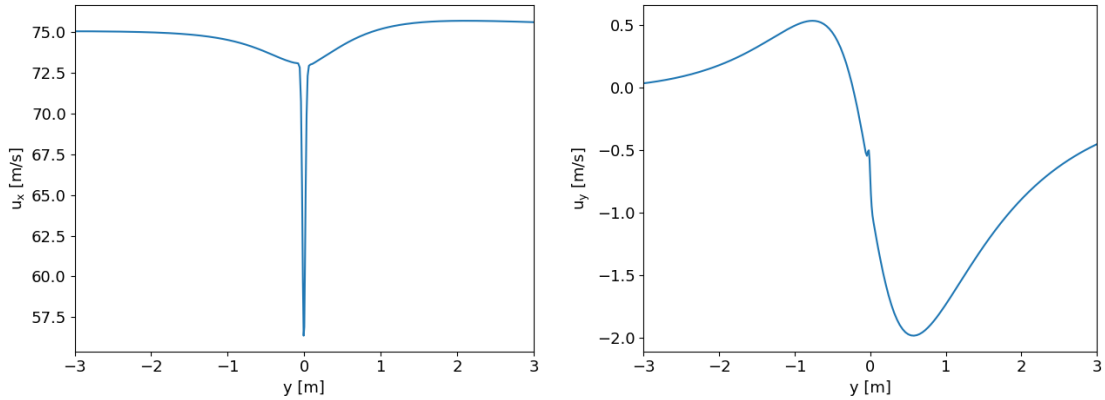

(a) Velocity in the axial direction.

(b) Velocity in the vertical direction.

Figure 5.3: Velocity profile 0.5 m behind the 1.84 m chord NACA 23013 airfoil wing at 0 degree angle of attack.

operating in free axial stream at 75 m/s and behind a wing with the wake from Figure 5.3 were made. From Figure 5.4 it can be concluded that the OASPL emitted by a propeller is influenced by the inflow velocity profile and generally increases when thrust is increased. Previous work has determined that at a given rotational velocity, both thrust and noise tend to increase when the propeller operates in a wake [91, 92]. However, results are seldom presented at constant thrust conditions. It is also important to highlight that the OASPL is most influenced by the inflow at lower thrust levels. As the thrust level increases, the induction factors, and therefore the induced velocities, also increase which reduces the impact of the initial airflow velocity profile and leads to a convergence of the free stream and wing wake results.

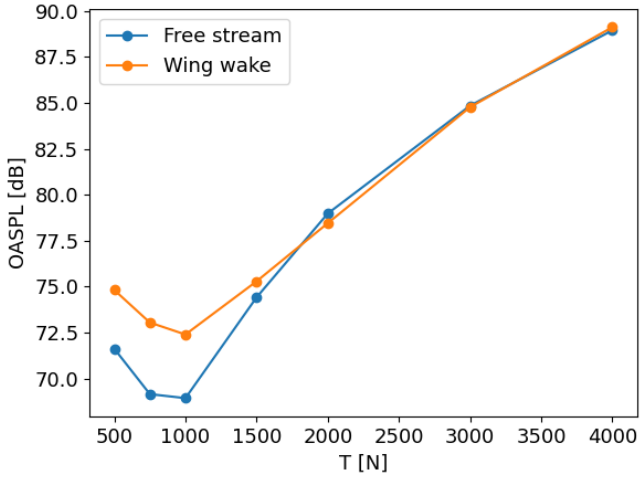

Figure 5.4: OASPL at different thrust levels. Measured in Position A.

5.3 Building the Surrogates

Having concluded that the OASPL tends to increase when operating in a wake, four surrogates were built for a propeller operating in the wake conditions previously described at 1500 N of thrust. These surrogates were built with the boundaries from Table 5.1 at the observer positions from Figure 5.2.

The selection of the best number of query points is fundamental to produce a good but efficient surrogate. In order to better understand the model and the surrogate, a study where different surrogates in position A were generated using a range of LHS of different sizes and then tested was performed. The testing of all surrogates was made against the same set of 50 space filling samples gathered from the model. Figure 5.5 shows that although there is a clear trend of model refinement as the number of points increases, there is some degree of volatility in the evaluation parameters. This is a direct result of the nature of the process of generating the LHS. Since every LHS is unique and random, it is possible for a sampling plan to be ”lucky” and hit more relevant points in the engineering function while a different sampling plan with the same number of points might be ”unlucky” and hit less relevant points in the engineering function. With the increase in the number of points, in addition to the increased overall fidelity, the influence of ”luck” decreases and the volatility also decreases.

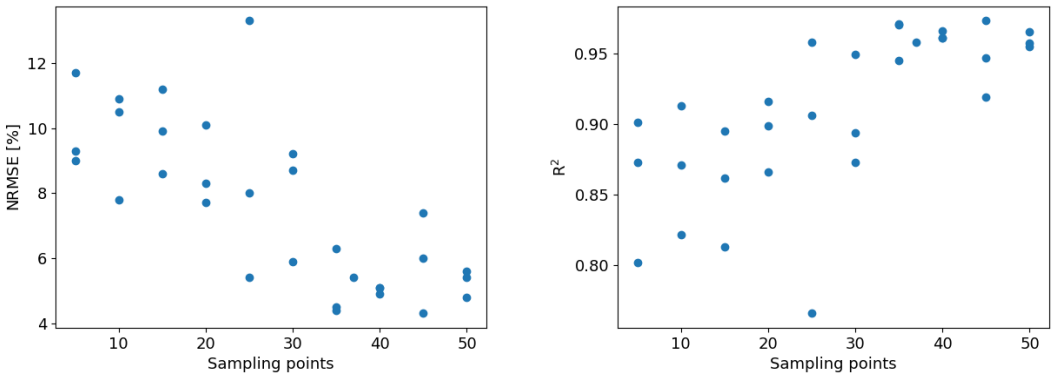

(a) Normalized RMSE.

(b) Correlation coefficient.

Figure 5.5: Surrogate A evaluation for different sets of query points.

In order to ensure the surrogate would meet the threshold criteria of normalised RMSE up to 10% and a correlation coefficient greater than 0.9 [42], it was decided to use 50 sample points in the surrogates. The validation process with a space filling set of samples of 25% the number of points was still performed to ensure every surrogate met the criteria and

was not ”unlucky”. The validation results for the four surrogates used are organised in Table 5.2.

Table 5.2: Surrogate testing results.

Surrogate	r^2	NRMSE
A	0.990	4.14 %
B	0.920	9.02 %
C	0.956	6.82 %
D	0.912	8.16 %

5.4 Using the Surrogates

A detailed view of the surrogates' output in the complete design space is represented in Appendix A.

5.4.1 Number of Propeller Blades (B)

One would expect that the increase in the number of blades would lead to a decrease in OASPL as the blade loading decreases. This, however is not always the case. In Figure 5.6 the OASPL for different numbers of blades at different blade radii is compared. For larger radii, an increase in the number of blades leads to a considerable reduction in noise which is a direct result of the decrease in blade loading and, therefore the decrease in loading noise. For smaller blade radii, this is not guaranteed, indicating that at a certain point, the loading noise decrease caused by the increasing number of blades is offset by the increase in thickness noise caused by the increase in the volume of air displaced by the propeller. Despite being represented for $CR = 1$ and $TI = 0$, this tendency is observed in other conditions.

5.4.2 Chord Ratio (CR)

The optimal chord ratio is highly dependent on the number of blades. Typically, smaller chord ratios are favoured with the increase of the number of blades as represented in Figure 5.7. This is a result of maintaining a balance between loading noise and thickness noise. With the increase in the number of blades, blade loading decreases and the loading

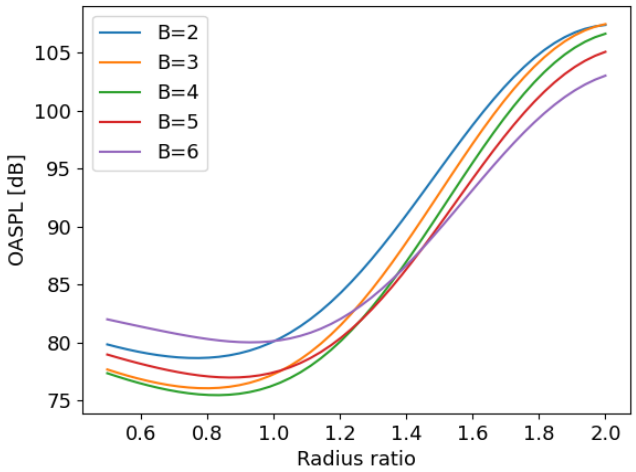

Figure 5.6: OASPL at different blade counts and blade radii. Surrogate A; $TI = 0$; $CR = 1$.

noise is reduced but the thickness noise is increased. This increase in thickness noise may be offset by the reduction in blade chord which in itself increases loading noise. The balance between these two leads to an optimal region.

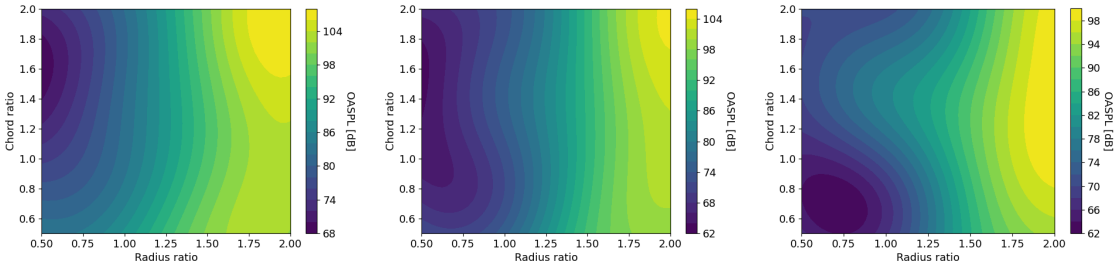

(a) 2 Blades. (b) 4 Blades. (c) 6 Blades.

Figure 5.7: OASPL at different design specifications. Surrogate A; $TI = 5$.

5.4.3 Radius Ratio (RR)

In general, lower blade radii are favoured as can be observed in Figures 5.6 and 5.7. This result is atypical as larger propeller are usually known for being more silent due to the decreased disk loading [9]. However, the larger blade diameter also increases the volume of air displaced by the propellers and, therefore, the thickness noise. In this particular case, with this base geometry, inflow velocity profile and thrust requirement, the reduction of thickness noise tends to be more advantageous than the increase in loading noise caused by the decrease in propeller diameter.

5.4.4 Twist Increment (TI)

An increase in blade incidence tends to reduce the OASPL in the vast majority of cases such as in Figure 5.8. With the higher blade incidence the propeller is able to generate the same thrust, and similar loading noise, at a lower angular velocity which will lead to a decrease in thickness noise as less air is displaced by the volume of the blades in a given time period.

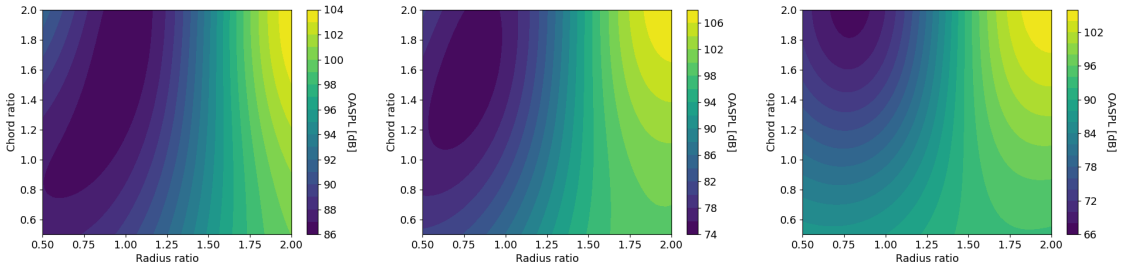

(a) $TI = -10$. (b) $TI = 0$. (c) $TI = 10$.

Figure 5.8: OASPL at different design specifications. Surrogate B; $B = 2$.

5.4.5 Optimisation

One of the purposes of this tool is its application in optimisation problems. As such, it was decided to find the geometry that would minimise the noise produced by a propeller. The optimisation tool used was the same evolutionary algorithm used to optimise the parameters $\{\theta\}$ and $\{p\}$.

As a first approach, each surrogate was minimised independently. The results, organised in Table 5.3, show that the optimal propeller in terms of noise production is very dependent on the position of the observer. Surrogate A, which corresponds to an observer in the propeller plane, was optimised to a propeller with the maximum number of blades and small blade chord and radius. The other propellers followed the same tendency of increased blade chord, reduced blade radius, increased blade incidence. All surrogates returned a different optimal number of blades.

These results show that the optimisation of a propeller's geometry cannot be done independently of the position of the observer. To further elaborate this point the optimal propeller from Surrogate A was used in Surrogate B and produced 76.61 dB of noise. Despite being the best performing propeller in observer position A, this propeller performs

Table 5.3: Individual surrogate optimisation results.

Surrogate	OASPL [dB]	B	CR	RR	TI [deg]
A	61.18	6	0.66	0.72	2.11
B	64.79	3	1.95	0.76	10.00
C	59.90	2	1.76	0.64	10.00
D	57.81	4	1.39	0.83	10.00

12 dB worse at position B than the optimal propeller at that position.

To find the acoustically optimal propeller, all surrogates must be searched at the same time. As such, the optimisation process was modified to minimise the function in Eq. 5.1 which corresponds to the maximum OASPL of the four surrogates. This process resulted in the propeller from Table 5.4 which is the best compromise between the four propellers on Table 5.3.

$$f(A, B, C, D) = \max(OASPL_A, OASPL_B, OASPL_C, OASPL_D) \quad (5.1)$$

Table 5.4: Optimal propeller.

Variable	Value
Number of blades (B)	3
Chord ratio (CR)	1.84
Radius ratio (RR)	0.74
Twist increment (TI) [deg]	9.95

In Table 5.5, the noise produced by the optimal propeller in all four positions is presented. This propeller is only slightly louder than the best propeller from Surrogate B, however, it maintains its acoustic performance across all positions analysed.

Table 5.5: Optimal propeller acoustic performance at the test locations.

Surrogate	OASPL [dB]
A	65.00
B	65.00
C	63.22
D	63.86

5.5 Computing Time Comparison

An important measure to identify the benefits of using a surrogate is the comparison of the computing time required. As such, a comparison of the computing times for the case study was made.

Using the time durations from Table 5.6, Figure 5.9 was created. It is clear that computing the OASPL at a point in the design space using the surrogate is essentially instantaneous and therefore the usage of the surrogate will always be the more computationally efficient approach if the number of desired function points exceeds the number of points used to construct and validate the surrogate. In this particular case study, if the tool were to be used in a parametric study or optimisation problem, the number of points required would most likely exceed 62 and, therefore, using the surrogate would be the computationally most efficient approach.

Table 5.6: Computing time required at different stages.

Step	Computing time [s]
Compute OASPL directly at a point	187.5
Train and validate the surrogate	4.9
Compute OASPL with the surrogate at a point	0.004

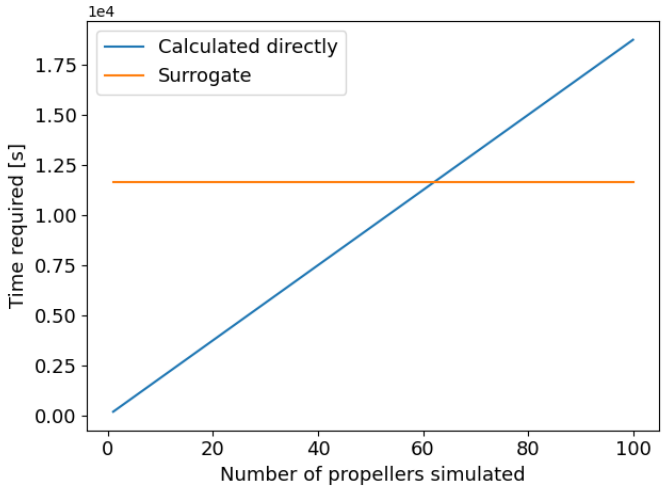

Figure 5.9: Required compute time for different numbers of simulated propellers.

A practical example is the calculation of the optimal propeller from Section 5.4.5 which required 1755 evaluations of each surrogate resulting in a total of $1755 \times 4 = 7020$ noise calculations and took $9.95\ s$ to perform. This results in 0.0014 s per calculation which is faster than the value presented in Table 5.6 as the evolutionary optimisation algorithm

takes advantage of parallel computing. Using the same proportion to the time from Table 5.6, it is estimated that the optimisation process would take $466406\ s$ or 5 days and 10 hours which highlights the computational efficiency advantages of the surrogate.

Chapter 6

Conclusions

6.1 Summary and Conclusions

The main objective of this dissertation was the creation of a tool capable of estimating the noise produced by a propeller under unsteady load conditions which are fundamental aspects of modern aircraft design problems due to the growing concerns about the environmental and social effects of aircraft noise and the increasing popularity of propeller driven unconventional aircraft designs which may place the propellers in the wake of structural components such as wings, pylons or fuselages. Another crucial functionality is the ability to produce quick accurate results in order to facilitate its usage in optimisation problems or parametric studies.

The approach to the problem began with the disregarding of the effects of broadband noise, and utilisation of Farassat's 1A formulation of the Ffowcs Williams and Hawkings equation to estimate the harmonic noise. This state of the art formulation, which is used in several propeller noise prediction tools, requires the input of detailed pressure data on the surface of the propellers which is usually obtained using slow, complicated simulations. As this was incompatible with the nature of the tool, a compact formulation of the Farassat 1A formulation which only requires the input of a radial-wise distributed force was used. The calculation of this load was done through a modified Blade Element Momentum theory capable of being used in non axial flow conditions.

Despite the efforts to simplify the model and maintain high computational efficiency, the model did not meet the intended efficiency and an Ordinary Kriging surrogate was used to interpolate the model data from a Latin Hypercube sampling plan in a design space consisting of four propeller design variables: Number of blades; Chord ratio; Radius ratio; and Twist increment. This surrogate allows the quick, accurate calculation of the overall sound pressure level of any propeller in the design space, as long as the testing criteria of the surrogate is met.

Independent validation of the different functionality of the python computer code was performed against several experimental and numerical data from the literature. For these validation efforts, extra functionality, such as the Power Spectral Density calculation module was added to the code and techniques such as photographic propeller geometry measurement were performed. The surrogate module was also tested against a modified Branin function where the effect of optimising different Kriging parameters and the number of sampling points has on the precision of the surrogate was studied.

The tool was then used in an example case study. The process began with the calculation of the wake behind an airfoil in flight using Ansys Fluent. This velocity profile was then used to compare the effects of operating in and outside of a wake at different levels of thrust. In this test, it was observed that for an observer in the propeller plane directly below the propeller hub, the operation in a wake causes an increase in OASPL up to a certain thrust level. Beyond this point, the OSAPL generated by both in-wake of free flow operation is very similar. This process was followed by the creation of four different surrogates in different relative positions to the propeller which were operating in the same airfoil wake. Direct observation of the function lead to the conclusion that the effects of the four variables in the OASPL produced was not independent. Despite this dependence, several trends were observed such as the moderate increase in the number of blades, slight decrease in propeller radius, increase in propeller chord and increase in blade incidence. These observations were followed with an optimisation study where an evolutionary algorithm was used to find the optimal propeller. As a first approach, each of the four surrogates were optimised independently for minimum OASPL which lead to very distinct optimal propellers indicating that the optimal geometry is highly dependent on the position of the observer. Following this result, all four surrogates were optimised simultaneously which resulted in a balance between all four propellers from the individual optimisation and a slight increase in maximum OASPL. The speed advantages of the surrogate were also demonstrated as the optimisation process took 9.95 seconds which is considerably faster than the estimated 5 days and 10 hours using the direct calculation model.

6.2 Future Works

Regarding future works, the integration of this tool in a multidisciplinary aircraft analysis code and its usage in aircraft optimisation problems could be valuable. In addition, the creation of a parallel model to evaluate the performance impact of the geometry changes caused by the noise optimisation is of great interest.

Bibliography

[1] D. P. Thipphavong, R. Apaza, B. Barmore, V. Battiste, B. Burian, Q. Dao, M. Feary, S. Go, K. H. Goodrich, J. Homola, *et al.*, "Urban air mobility airspace integration concepts and considerations," in *2018 Aviation Technology, Integration, and Operations Conference*, p. 3676, 2018. 1

[2] A. Mahashabde, P. Wolfe, A. Ashok, C. Dorbian, Q. He, A. Fan, S. Lukachko, A. Mozdzanowska, C. Wollersheim, S. R. Barrett, *et al.*, "Assessing the environmental impacts of aircraft noise and emissions," *Progress in Aerospace Sciences*, vol. 47, no. 1, pp. 15–52, 2011. 1

[3] S. Morrell, R. Taylor, and D. Lyle, "A review of health effects of aircraft noise," *Australian and New Zealand journal of public health*, vol. 21, no. 2, pp. 221–236, 1997. 1

[4] E. Lynam, "The emission of sound by airscrews," *Reports and memoranda*, vol. 624, pp. 3–12, 1919. 3

[5] A. Demming, "Noise from propellers with symmetrical sections at zero blade angle," *NACA TM*, vol. 679, 1937. 3

[6] W. Ernsthausen, "The source of propeller noise," 1937. Luftfahrtforschung. Translated as NACA TM 825. 3

[7] L. Gutin, "On the sound field of a rotating propeller," *Physikalische Zeitschrit der Sowjetinion: Physical magazine of the Soviet Union volume 9 number 1*, vol. 9, no. 1, 1948. 3

[8] I. Garrick and C. E. Watkins, "A theoretical study of the effect of forward speed on the free-space sound-pressure field around propellers," 1953. 3

[9] H. H. Hubbard, *Aeroacoustics of flight vehicles: theory and practice*, vol. 1. National Aeronautics and Space Administration, Office of Management, 1991. 3, 26, 58

[10] R. J. Pegg, "A summary and evaluation of semi-empirical methods for the prediction of helicopter rotor noise," *Unknow*, 1979. 3

[11] M. Lowson, "Thoughts on broad band noise radiation by a helicopter," *Wyle Laboratories Inc., Report WR*, pp. 68–20, 1968. 3

[12] H. H. Hubbard, *Propeller-noise charts for transport airplanes*, vol. 2968. National Advisory Committee for Aeronautics, 1953. 3

[13] R. Schlegel, R. King, and H. Mull, "Helicopter rotor noise generation and propagation," tech. rep., UNITED TECHNOLOGIES CORP STRATFORD CT SIKORSKY AIRCRAFT DIV, 1966. 3

[14] C. L. Munch *et al.*, "Prediction of v/stol noise for application to community noise exposure," tech. rep., United States. Dept. of Transportation. Office of the Secretary, 1973. 3

[15] T. F. Brooks, D. S. Pope, and M. A. Marcolini, *Airfoil self-noise and prediction*, vol. 1218. National Aeronautics and Space Administration, Office of Management ..., 1989. 3

[16] R. WOODWARD, "Measured noise of a scale model high speed propeller at simulated takeoff/approach conditions," in *25th AIAA Aerospace Sciences Meeting*, p. 526, 1987. 4

[17] W. Dobrzynski, H. Heller, J. Powers, and J. Densmore, "Dfvlr/faa propeller noise tests in the german-dutch wind tunnel dnw," *DFVLR-IB*, vol. 129, no. 86, p. 3, 1986. 4

[18] J. E. Ffowcs Williams and D. L. Hawkings, "Sound generation by turbulence and surfaces in arbitrary motion," *Philosophical Transactions of the Royal Society of London. Series A, Mathematical and Physical Sciences*, vol. 264, no. 1151, pp. 321–342, 1969. 4

[19] M. J. Lighthill, "On sound generated aerodynamically i. general theory," *Proceedings of the Royal Society of London. Series A. Mathematical and Physical Sciences*, vol. 211, no. 1107, pp. 564–587, 1952. 4

[20] F. Farassat, *Theory of noise generation from moving bodies with an application to helicopter rotors*. National Aeronautics and Space Administration, 1975. 5

[21] F. Farassat and G. P. Succi, "A review of propeller discrete frequency noise prediction technology with emphasis on two current methods for time domain calculations," *Journal of Sound and Vibration*, vol. 71, no. 3, pp. 399–419, 1980. 5

[22] F. Farassat, "Derivation of formulations 1 and 1a of farassat," tech. rep., 2007. 5

[23] D. B. Hanson and M. R. Fink, "The importance of quadrupole sources in prediction of transonic tip speed propeller noise," *Journal of Sound and Vibration*, vol. 62, no. 1, pp. 19–38, 1979. 5

[24] W. E. Zorumski and D. S. Weir, "Aircraft noise prediction program theoretical manual: Propeller aerodynamics and noise," *Unknown*, 1986. 5

[25] F. Farassat, S. Padula, and M. Dunn, "Advanced turboprop noise prediction based on recent theoretical results," *Journal of Sound and Vibration*, vol. 119, no. 1, pp. 53–79, 1987. 5

[26] K. S. Brentner, "Prediction of helicopter rotor discrete frequency noise: A computer program incorporating realistic blade motions and advanced acoustic formulation," *Unknow*, 1986. 5, 11

[27] K. S. Brentner, G. A. Bres, G. Perez, and H. E. Jones, "Maneuvering rotorcraft noise prediction: A new code for a new problem," 2002. 5

[28] F. Farassat, "Theoretical analysis of linearized acoustics and aerodynamics of advanced supersonic propellers," 1985. 5

[29] M. H. Dunn and G. Tarkenton, "Computational methods in the prediction of advanced subsonic and supersonic propeller induced noise: Asspin users' manual," 1992. 5

[30] G. Brès, K. Brentner, G. Perez, and H. Jones, "Maneuvering rotorcraft noise prediction," *Journal of Sound and Vibration*, vol. 275, no. 3-5, pp. 719–738, 2004. 6, 7

[31] W. M. J. Rankine and R. E. Froude, "On the mechanical principles of the action of propellers," *Transactions of the Institution of Naval Architects*, 1889. 7

[32] S. Drzewiecki, *Bulletin de l'Association technique maritime*. 1892. 7

[33] H. Glauert, "Airplane propellers," in *Aerodynamic theory*, pp. 169–360, Springer, 1935. 7, 8, 15

[34] A. Betz, "Screw propellers with minimum loss of energy," *Norchr. Der K. Gesellschaft der Nissenschaften zu Goettingen*, no. 193, 1920. 7

[35] G. J. Leishman, *Principles of helicopter aerodynamics with CD extra*. Cambridge university press, 2006. 7

[36] H. Glauert, "A general theory of the autogyro," tech. rep., HM Stationery Office, 1926. 8

[37] D. M. Pitt and D. A. Peters, "Theoretical prediction of dynamic-inflow derivatives," 1980. 8

[38] H. Snel and J. Schepers, "Joint investigation of dynamic inflow effects and implementation of an engineering method," 1995. 8

[39] P. J. Moriarty and A. C. Hansen, "Aerodyn theory manual," tech. rep., National Renewable Energy Lab., Golden, CO (US), 2005. 8, 13, 16

[40] G. Matheron, "Principles of geostatistics," *Economic geology*, vol. 58, no. 8, pp. 1246–1266, 1963. 9

[41] D. G. Krige, "A statistical approach to some basic mine valuation problems on the witwatersrand," *Journal of the Southern African Institute of Mining and Metallurgy*, vol. 52, no. 6, pp. 119–139, 1951. 9

[42] A. Forrester, A. Sobester, and A. Keane, *Engineering design via surrogate modelling: a practical guide*. John Wiley & Sons, 2008. 9, 10, 18, 19, 21, 22, 31, 48, 49, 56

[43] M. R. Kianifar and F. Campean, "Performance evaluation of metamodelling methods for engineering problems: towards a practitioner guide," *Structural and Multidisciplinary Optimization*, vol. 61, no. 1, pp. 159–186, 2020. 9

[44] R. Yondo, E. Andrés, and E. Valero, "A review on design of experiments and surrogate models in aircraft real-time and many-query aerodynamic analyses," *Progress in Aerospace Sciences*, vol. 96, pp. 23–61, 2018. 9

[45] W. D. Wallis and J. C. George, *Introduction to combinatorics*. CRC press, 2016. 9

[46] B. Tang, "Orthogonal array-based latin hypercubes," *Journal of the American statistical association*, vol. 88, no. 424, pp. 1392–1397, 1993. 10

[47] Q. Y. Kenny, W. Li, and A. Sudjianto, "Algorithmic construction of optimal symmetric latin hypercube designs," *Journal of statistical planning and inference*, vol. 90, no. 1, pp. 145–159, 2000. 10

[48] M. E. Johnson, L. M. Moore, and D. Ylvisaker, "Minimax and maximin distance designs," *Journal of statistical planning and inference*, vol. 26, no. 2, pp. 131–148, 1990. 10

[49] M. D. Morris and T. J. Mitchell, "Exploratory designs for computational experiments," *Journal of statistical planning and inference*, vol. 43, no. 3, pp. 381–402, 1995. 10

[50] N. Bartoli, T. Lefebvre, S. Dubreuil, R. Olivanti, R. Priem, N. Bons, J. R. Martins, and J. Morlier, "Adaptive modeling strategy for constrained global optimization with application to aerodynamic wing design," *Aerospace Science and technology*, vol. 90, pp. 85–102, 2019. 10

[51] M. J. Sasena, P. Papalambros, and P. Goovaerts, "Exploration of metamodeling sampling criteria for constrained global optimization," *Engineering optimization*, vol. 34, no. 3, pp. 263–278, 2002. 10

[52] F. Farassat, "Linear acoustic formulas for calculation of rotating blade noise," *AIAA journal*, vol. 19, no. 9, pp. 1122–1130, 1981. 11

[53] L. L. Beranek *et al.*, *Acoustics*. 1954. 12

[54] C. H. Hansen, "Fundamentals of acoustics," *Occupational Exposure to Noise: Evaluation, Prevention and Control. World Health Organization*, pp. 23–52, 2001. 12

[55] J. W. Cooley and J. W. Tukey, "An algorithm for the machine calculation of complex fourier series," *Mathematics of computation*, vol. 19, no. 90, pp. 297–301, 1965. 12

[56] W. T. Cochran, J. W. Cooley, D. L. Favin, H. D. Helms, R. A. Kaenel, W. W. Lang, G. C. Maling, D. E. Nelson, C. M. Rader, and P. D. Welch, "What is the fast fourier transform?," *Proceedings of the IEEE*, vol. 55, no. 10, pp. 1664–1674, 1967. 12

[57] R. Oshana, "Overview of digital signal processing algorithms," *DSP Software Development Techniques for Embedded and Real-Time Systems*, pp. 59–121, 2006. 13

[58] M. Drela, "Xfoil: An analysis and design system for low reynolds number airfoils," in *Low Reynolds number aerodynamics*, pp. 1–12, Springer, 1989. 16

[59] A. Deperrois, "xflr5," 2003. `http://www.xflr5.tech/xflr5.htm`. 16

[60] M. Drela, "Xfoil 6.9 user primer," 2001. `http://web.mit.edu/drela/Public/web/xfoil/xfoil_doc.txt`, [Accessed: 8 April 2021]. 16

[61] M. A. Silvestre, J. P. Morgado, and J. Pascoa, "Jblade: a propeller design and analysis code," in *2013 International Powered Lift Conference*, p. 4220, 2013. 16, 33

[62] L. A. Viterna and R. D. Corrigan, "Fixed pitch rotor performance of large horizontal ax is wind turbines," in *NASA Lewis Research Center: Energy Production and Conversion Workshop, Cleveland, OH, United States January*, vol. 1, 1982. 16

[63] D. Laino and A. C. Hansen, "User's guide to the wind turbine aerodynamics computer software aerodyn.," tech. rep., 2002. 16

[64] A. Ning, "airfoilprep.py," 2012. `https://github.com/WISDEM/AirfoilPreppy/blob/master/airfoilprep/airfoilprep.py`, [Accessed: 30 April 2021]. 16

[65] M. A. Bouhlel, J. T. Hwang, N. Bartoli, R. Lafage, J. Morlier, and J. R. Martins, "A python surrogate modeling framework with derivatives," *Advances in Engineering Software*, vol. 135, p. 102662, 2019. 19

[66] R. Jin, W. Chen, and A. Sudjianto, "An efficient algorithm for constructing optimal design of computer experiments," in *International Design Engineering Technical Conferences and Computers and Information in Engineering Conference*, vol. 37009, pp. 545–554, 2003. 19

[67] P. Virtanen, R. Gommers, T. E. Oliphant, M. Haberland, T. Reddy, D. Cournapeau, E. Burovski, P. Peterson, W. Weckesser, J. Bright, *et al.*, "Scipy 1.0: fundamental algorithms for scientific computing in python," *Nature methods*, vol. 17, no. 3, pp. 261–272, 2020. 21, 29

[68] R. Storn and K. Price, "Differential evolution - a simple and efficient heuristic for global optimization over continuous spaces," *Journal of global optimization*, vol. 11, no. 4, pp. 341–359, 1997. 21

[69] J. Friedman, T. Hastie, R. Tibshirani, *et al.*, *The elements of statistical learning*, vol. 1. Springer series in statistics New York, 2001. 22

[70] F. R. Menter, "Two-equation eddy-viscosity turbulence models for engineering applications," *AIAA journal*, vol. 32, no. 8, pp. 1598–1605, 1994. 23

[71] D. Monk and E. A. Chadwick, "Comparison of turbulence models effectiveness for a delta wing at low reynolds numbers," in *7th European conference for aeronautics and space sciences (EUCASS)*, vol. 1303, 2017. 23

[72] D. B. Hanson, "Influence of propeller design parameters on far-field harmonic noise in forward flight," *AIAA Journal*, vol. 18, no. 11, pp. 1313–1319, 1980. 26

[73] ISO, "Standard atmosphere, iso 2533: 1975," 1975. 28

[74] S. C. Chapra and R. P. Canale, *Numerical methods for engineers*, vol. 1221. Mcgraw-hill New York, 2011. 29

[75] M. O. Hansen, "Aerodynamics and design of horizontal-axis wind turbines," in *Wind Energy Engineering*, pp. 161–184, Elsevier, 2017. 29

[76] K. S. Brentner, C. L. Burley, and M. A. Marcolini, "Sensitivity of acoustic predictions to variation of input parameters," *Journal of the American Helicopter Society*, vol. 39, no. 3, pp. 43–52, 1994. 29, 30

[77] J. Páscoa, J. Morgado, and M. Silvestre, "Validation of new formulations for propeller analysis," *Journal of Propulsion and Power*, vol. 31, no. 1, pp. 467–477, 2015. 33

[78] J. P. S. Morgado, *Development of an open source software tool for propeller design in the MAAT project*. PhD thesis, University of Beira Interior, 2016. 33, 34

[79] C. N. Adkins and R. H. Liebeck, "Design of optimum propellers," *Journal of Propulsion and Power*, vol. 10, no. 5, pp. 676–682, 1994. 33, 34

[80] B. Montgomerie, "Methods for root effects, tip effects and extending the angle of attack range to {+-} 180 deg., with application to aerodynamics for blades on wind turbines and propellers," 2004. 34

[81] S. Xiang, Y.-q. Liu, G. Tong, W.-p. Zhao, S.-x. Tong, and Y.-d. Li, "An improved propeller design method for the electric aircraft," *Aerospace Science and Technology*, vol. 78, pp. 488–493, 2018. 35

[82] T. Theodorsen, G. W. Stickle, and M. Brevoort, "Characteristics of six propellers including the high-speed range," *Annual Report-National Advisory Committee for Aeronautics*, vol. 401, 1937. 36, 37, 44, 53

[83] H. C. McLemore and M. D. Cannon, "Aerodynamic investigation of a four-blade propeller operating through an angle-of-attack range from 0 to 180 degrees," 1954. 38, 39

[84] H. B. Freeman, *The effect of small angles of Yaw and Pitch on the characteristics of airplane propellers*. National Advisory Committee for Aeronautics, 1931. 40

[85] A. Zarev and R. Green, "Experimental investigation of the effect of yaw angle on the inflow of a two-bladed propeller," *Aerospace Science and Technology*, vol. 103, p. 105940, 2020. 42, 43

[86] D. WEIR and J. POWERS, "Comparisons of predicted propeller noise with windtunnel and flyoverdata," in *25th AIAA Aerospace Sciences Meeting*, p. 527, 1987. 43, 44, 45

[87] H. Wang, B. Zang, A. Celik, D. Rezgui, and M. Azarpeyvand, "An experimental investigation of propeller noise in forward flow," in *25th AIAA/CEAS Aeroacoustics Conference*, p. 2620, 2019. 45, 46

[88] "Engineering design process used to develop apc propellers." `https://www.apcprop.com/technical-information/engineering/`. Accessed: 25/05/2021. 45, 47

[89] J. B. Brandt, R. W. Deters, G. K. Ananda, and M. S. Selig, "Uiuc propeller database," *University of Illinois at Urbana-Champaign, retrieved from https://m-selig.ae.illinois.edu/props/propDB.html*. Downloaded on 30/05/2021. 45, 46, 47

[90] L. Marino, "Experimental analysis of uav propeller noise," in *16th AIAA/CEAS Aeroacoustics Conference*, p. 3854, 2010. 46, 49

[91] T. Sinnige, D. Ragni, A. M. Malgoezar, G. Eitelberg, and L. L. Veldhuis, "Apian-inf: an aerodynamic and aeroacoustic investigation of pylon-interaction effects for pusher propellers," *CEAS Aeronautical Journal*, vol. 9, no. 2, pp. 291–306, 2018. 55

[92] Y. Yauwenas, J. R. Fischer, D. Moreau, and C. J. Doolan, "The effect of inflow disturbance on drone propeller noise," in *25th AIAA/CEAS Aeroacoustics Conference*, p. 2663, 2019. 55

Appendix A

Detailed Visualisation of the Surrogates

A.1 Surrogate A

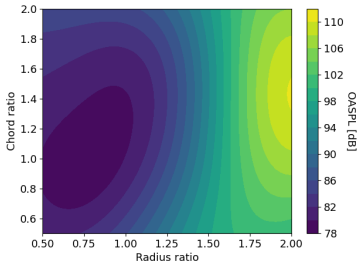

2 Blades.

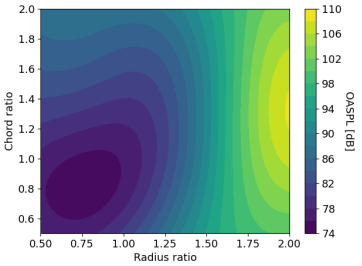

4 Blades.

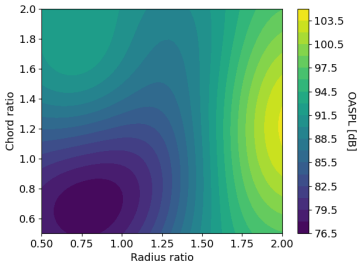

6 Blades.

Twist Increment = -10.

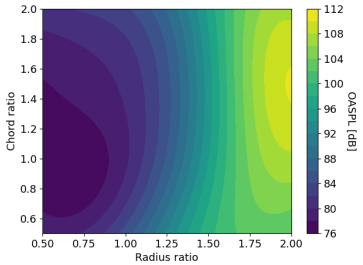

2 Blades.

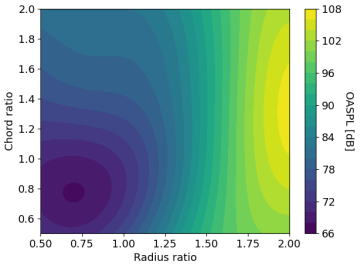

4 Blades.

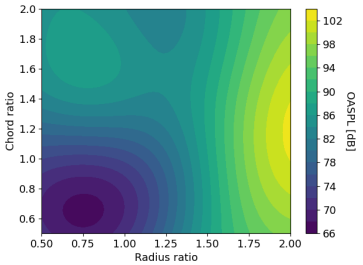

6 Blades.

Twist Increment = -5.

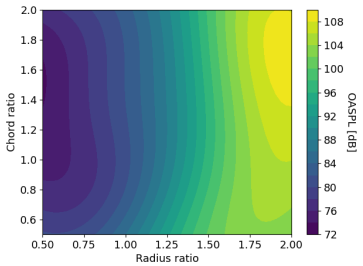

2 Blades.

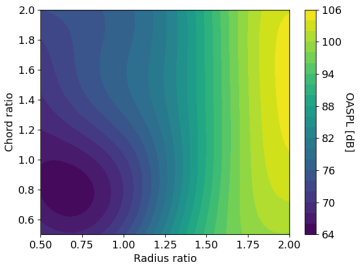

4 Blades.

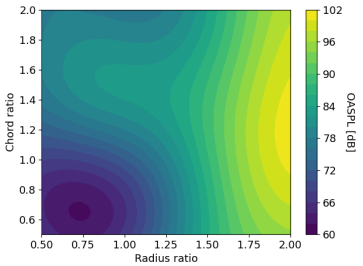

6 Blades.

Twist Increment = 0.

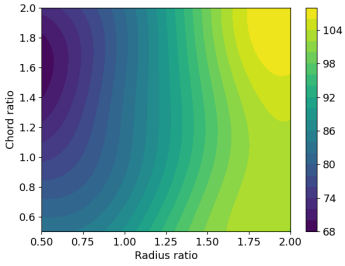

2 Blades.

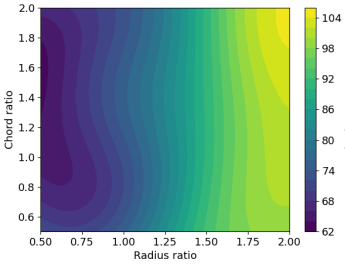

4 Blades.

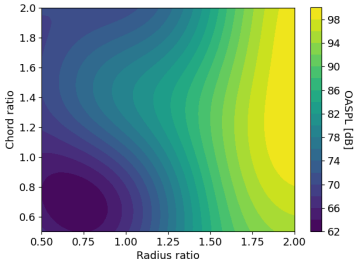

6 Blades.

Twist Increment = 5.

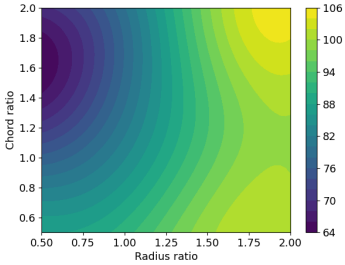

2 Blades.

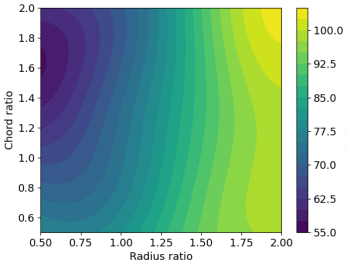

4 Blades.

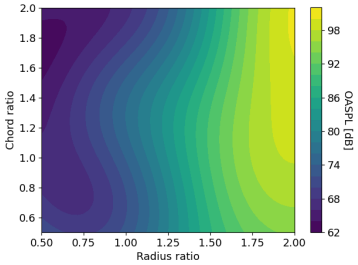

6 Blades.

Twist Increment = 10.

A.2 Surrogate B

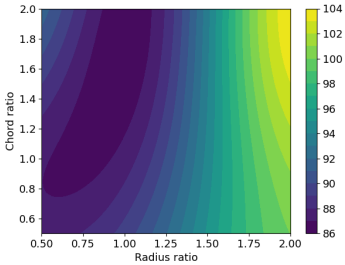

2 Blades.

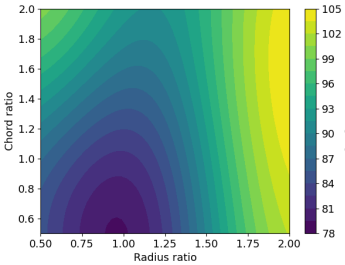

4 Blades.

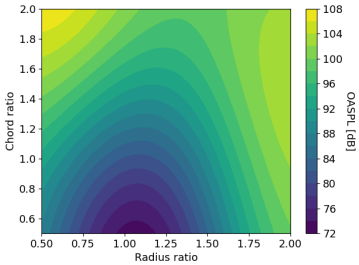

6 Blades.

Twist Increment = -10.

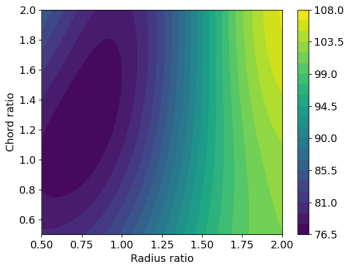

2 Blades.

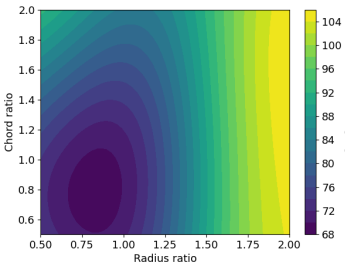

4 Blades.

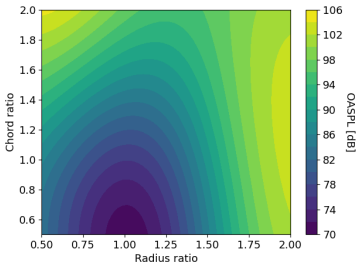

6 Blades.

Twist Increment = -5.

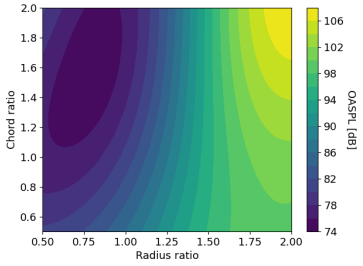

2 Blades.

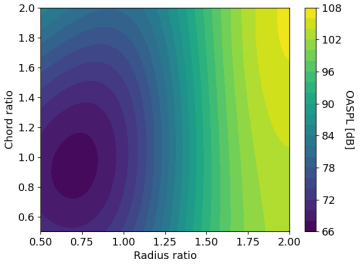

4 Blades.

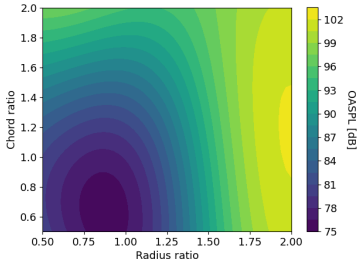

6 Blades.

Twist Increment = 0.

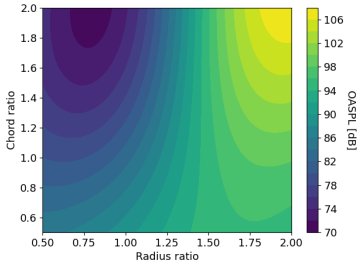

2 Blades.

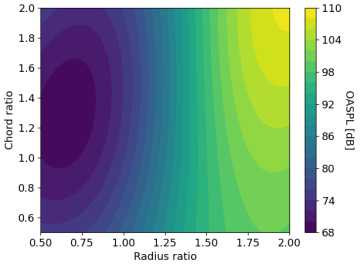

4 Blades.

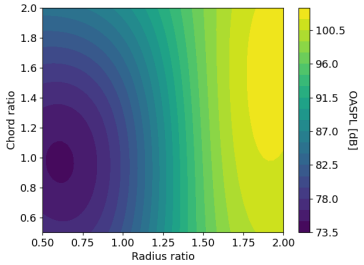

6 Blades.

Twist Increment = 5.

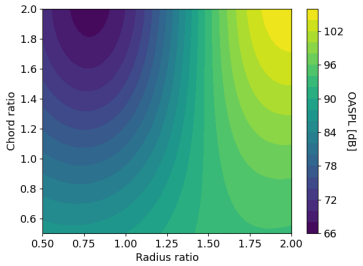

2 Blades.

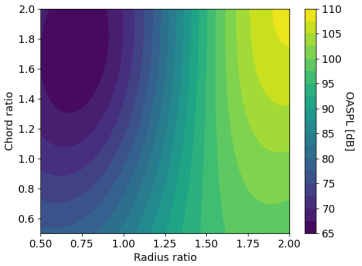

4 Blades.

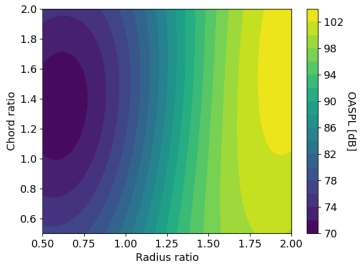

6 Blades.

Twist Increment = 10.

A.3 Surrogate C

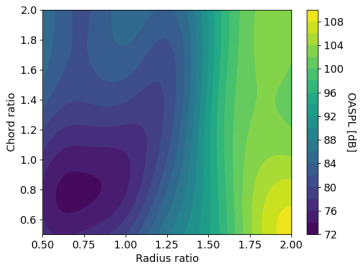

2 Blades.

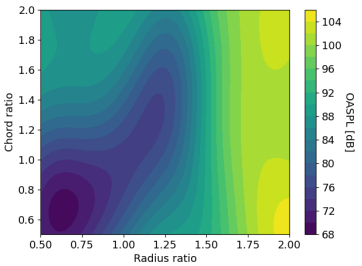

4 Blades.

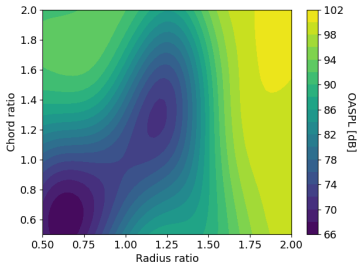

6 Blades.

Twist Increment = −10.

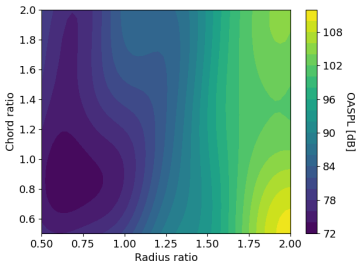

2 Blades.

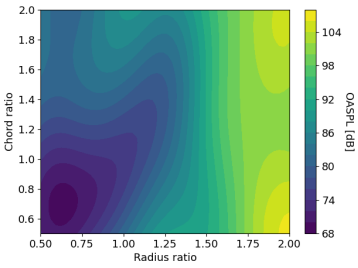

4 Blades.

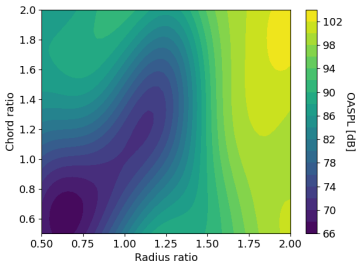

6 Blades.

Twist Increment = -5.

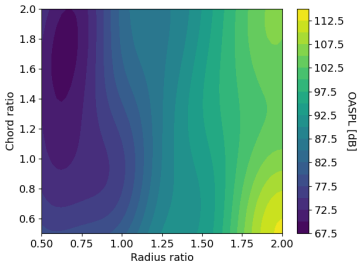

2 Blades.

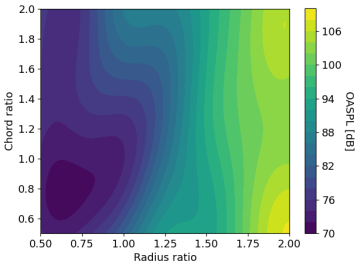

4 Blades.

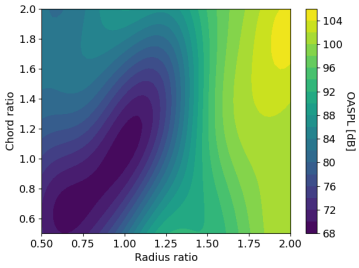

6 Blades.

Twist Increment = 0.

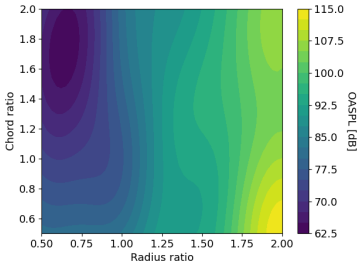

2 Blades.

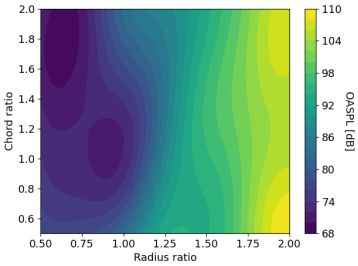

4 Blades.

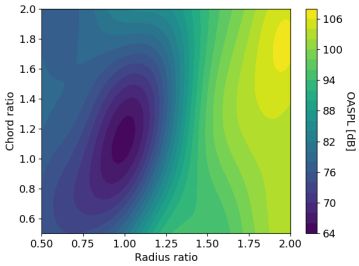

6 Blades.

Twist Increment = 5.

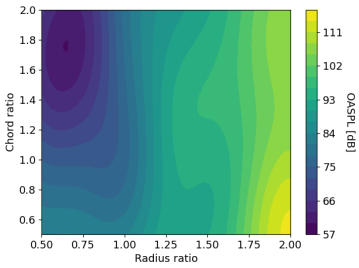

2 Blades.

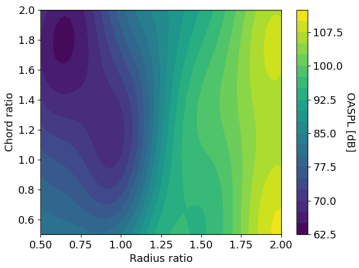

4 Blades.

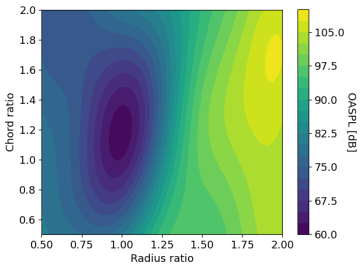

6 Blades.

Twist Increment = 10.

A.4 Surrogate D

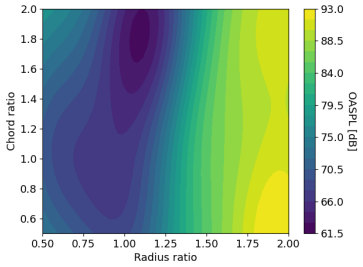

2 Blades.

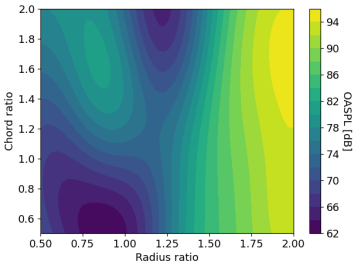

4 Blades.

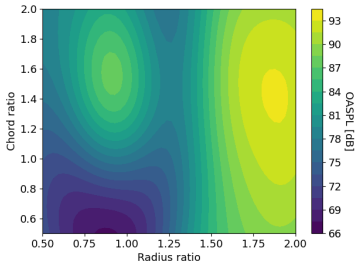

6 Blades.

Twist Increment = -10.

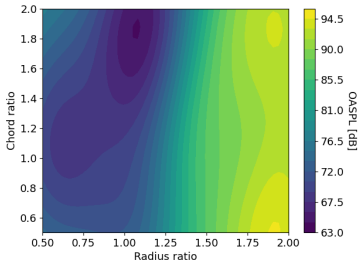

2 Blades.

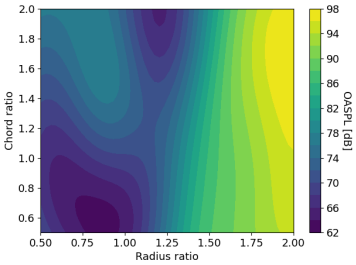

4 Blades.

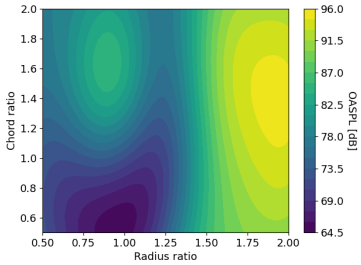

6 Blades.

Twist Increment = -5.

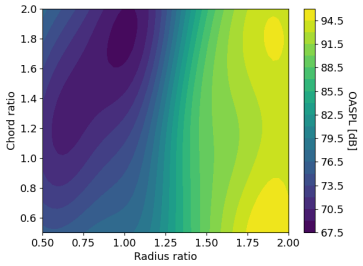

2 Blades.

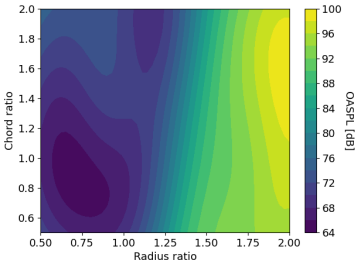

4 Blades.

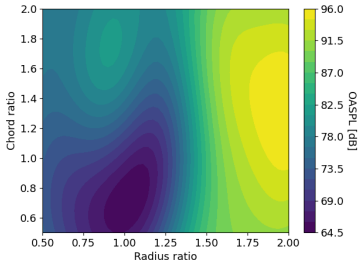

6 Blades.

Twist Increment = 0.

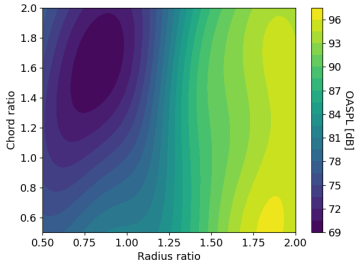

2 Blades.

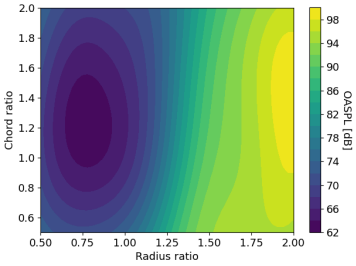

4 Blades.

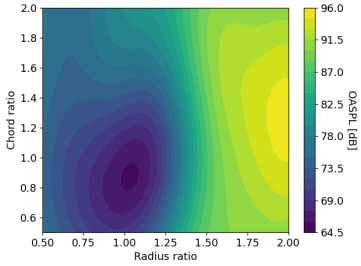

6 Blades.

Twist Increment = 5.

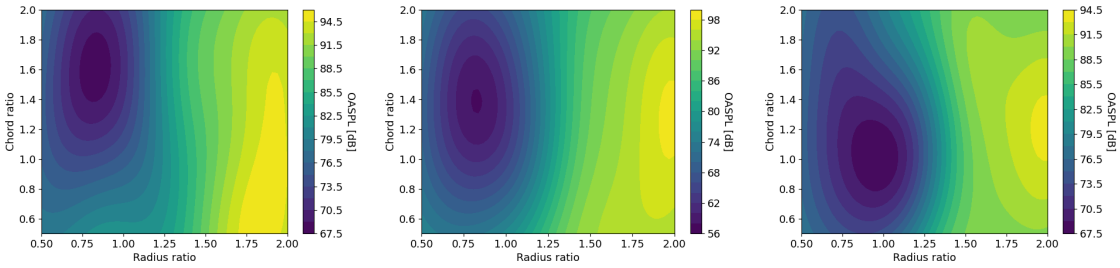

2 Blades. 4 Blades. 6 Blades.

Twist Increment = 10.

Appendix B

Additional Results From This Work

B.1 Computer Code

The tool was made open source with the GNU General Public Licence and is available in a Github repository for direct use or further development: `https://zenodo.org/badge/latestdoi/381293929`.

B.2 Conference Paper

Surrogate Modelling of Propeller Noise in Unsteady Load Conditions
P. M. Neto and P. V. Gamboa
AeroBest 2021, Lisbon, Portugal, July 2021